



Published in final edited form as:

Cell Rep. 2021 November 02; 37(5): 109934. doi:10.1016/j.celrep.2021.109934.

## RNA-binding protein FXR1 drives cMYC translation by recruiting eIF4F complex to the translation start site

Jasmine George<sup>1</sup>, Yongsheng Li<sup>2</sup>, Ishaque P. Kadamberi<sup>1</sup>, Deepak Parashar<sup>1</sup>, Shirng-Wern Tsaih<sup>1</sup>, Prachi Gupta<sup>1</sup>, Anjali Geethadevi<sup>1</sup>, Changliang Chen<sup>1</sup>, Chandrima Ghosh<sup>3</sup>, Yunguang Sun<sup>4</sup>, Sonam Mittal<sup>1</sup>, Ramani Ramchandran<sup>5</sup>, Hallgeir Rui<sup>4</sup>, Gabriel Lopez-Berestein<sup>6,7</sup>, Cristian Rodriguez-Aguayo<sup>6,7</sup>, Gustavo Leone<sup>8,12</sup>, Janet S. Rader<sup>1</sup>, Anil K. Sood<sup>7,9</sup>, Madhusudan Dey<sup>3</sup>, Sunila Pradeep<sup>1,10,11,12</sup>, Pradeep Chaluvally-Raghavan<sup>1,10,11,12,13,\*</sup>

<sup>1</sup>Department of Obstetrics and Gynecology, Medical College of Wisconsin, Milwaukee, WI 53226, USA

<sup>2</sup>Key Laboratory of Tropical Translational Medicine of Ministry of Education, College of Biomedical Information and Engineering, Hainan Medical University, Haikou 571199, China

<sup>3</sup>Department of Biological Sciences, University of Wisconsin, Milwaukee, WI 53211, USA

<sup>4</sup>Department of Pathology, Medical College of Wisconsin, Milwaukee, WI 53226, USA

<sup>5</sup>Department of Pediatrics, Medical College of Wisconsin, Milwaukee, WI 53226, USA

<sup>6</sup>Department of Experimental Therapeutics, University of Texas MD Anderson Cancer Center, 1515 Holcombe Blvd., Houston, TX 77030, USA

<sup>7</sup>Center for RNA Interference and Non-Coding RNA, University of Texas MD Anderson Cancer Center, 1515 Holcombe Blvd., Houston, TX 77030, USA

<sup>8</sup>Department of Biochemistry, Medical College of Wisconsin, Milwaukee, WI 53226, USA

<sup>9</sup>Department of Gynecologic Oncology and Reproductive Medicine and Cancer Biology, University of Texas MD Anderson Cancer Center, 1515 Holcombe Blvd., Houston, TX 77030, USA

<sup>10</sup>Department of Physiology, Medical College of Wisconsin, Milwaukee, WI 53226, USA

This is an open access article under the CC BY-NC-ND license (<http://creativecommons.org/licenses/by-nc-nd/4.0/>).

\*Correspondence: pchaluvally@mcw.edu.

### AUTHOR CONTRIBUTIONS

P.C.R. conceived the study, generated hypotheses, and designed the experiments. J.G. designed and performed most of the experiments, including cell cultures, animal experiments, qPCR, microscopy, immunoblots, REMSA, PLA, statistical analyses, preparing figures, and the drafting the manuscript. Y.L. and S.-W.T. performed all the bioinformatics and computational analysis for this study. D.P., A.G., P.G., C.C., or S.M. and I.P.K. assisted on animal experiments, animal imaging or *in vitro* experiments. S.P. and P.C.R. designed the animal experiments. S.P. provided scientific feedback and assisted with manuscript preparation. Y.S. and H.R. assisted on IHC scanning and pathology analysis consultations. G.L.-B., C.R.-A., and A.K.S. incorporated siRNA into nanoliposomes. H.R., J.S.R., R.R., and M.D. edited the manuscript and provided comments. C.G. and M.D. assisted with polysome fractionation and translational experiments. P.C.R. provided scientific direction, established collaborations, prepared the manuscript with J.G., and allocated funding for the work.

### SUPPLEMENTAL INFORMATION

Supplemental information can be found online at <https://doi.org/10.1016/j.celrep.2021.109934>.

### DECLARATION OF INTERESTS

The authors declare no competing interests.

<sup>11</sup>Center of Systems Molecular Medicine, Medical College of Wisconsin, Milwaukee, WI 53226, USA

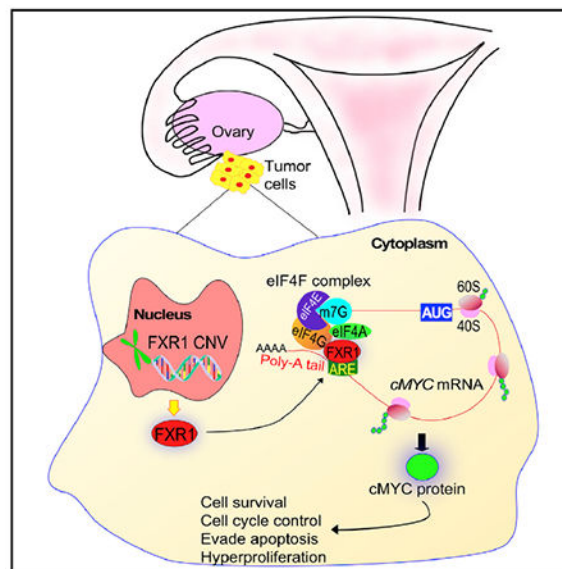
<sup>12</sup>Medical College of Wisconsin Cancer Center, Milwaukee, WI 53226, USA

<sup>13</sup>Lead contact

## SUMMARY

Fragile X-related protein-1 (FXR1) gene is highly amplified in patients with ovarian cancer, and this amplification is associated with increased expression of both *FXR1* mRNA and protein. FXR1 expression directly associates with the survival and proliferation of cancer cells. Surface sensing of translation (SUnSET) assay demonstrates that FXR1 enhances the overall translation in cancer cells. Reverse-phase protein array (RPPA) reveals that cMYC is the key target of FXR1. Mechanistically, FXR1 binds to the AU-rich elements (ARE) present within the 3' untranslated region (3' UTR) of cMYC and stabilizes its expression. In addition, the RGG domain in FXR1 interacts with eIF4A1 and eIF4E proteins. These two interactions of FXR1 result in the circularization of *cMYC* mRNA and facilitate the recruitment of eukaryotic translation initiation factors to the translation start site. In brief, we uncover a mechanism by which FXR1 promotes cMYC levels in cancer cells.

## Graphical abstract



## In brief

George et al. demonstrate that FXR1 binds to the AREs within the 3' UTR of *MYC* mRNA and improves its stability. The authors also show that the RGG domain of FXR1 interacts with eIF4A1 and eIF4E and facilitates recruitment of the eIF4F complex to translation initiation sites for cMYC translation.

## INTRODUCTION

Copy number variations (CNVs), such as genomic amplification, copy number gain, or deletion, are frequent events in ovarian cancer (Cancer Genome Atlas Research Network, 2011). Among CNVs, amplification of the 3q26 locus is seen in ~30% of high-grade serous ovarian cancers (HGSOC). Previously, it was demonstrated that many genes, such as *PI3KCA* (Shayesteh et al., 1999) and *EVII* (Wang et al., 2015), are parts of the 3q26 locus that contribute to the development and progression of ovarian and other cancers. Recently, our group reported that non-coding RNAs, such as the microRNAs miR569 and miR551b that are amplified as part of the 3q26.2 locus, contribute to the oncogenesis and progression of breast and ovarian cancers (Chaluvally-Raghavan et al., 2014, 2016; Parashar et al., 2019). Collectively, these studies suggest that 3q26 is important in ovarian and other cancers because many genes in this amplicon promote oncogenesis either individually or by cooperating with other genes in this locus or with their downstream targets or actions.

By analyzing high-resolution single nucleotide polymorphism (SNP) array data of the Cancer Genome Atlas (TCGA), we determined that fragile X-related protein 1 (FXR1), which is located in the 3q26.3 chromosomal locus, is highly amplified or copy-gained in ovarian cancer and many other cancers, including squamous cell carcinoma of the lung, cervix, head, and neck. FXR1, which is highly conserved in mammals (Kirkpatrick et al., 1999), is a member of the fragile X-related (FXR) family of RNA-binding proteins (RBPs). Studies have shown that FXR1 is a key promoter of tumor progression, which is critical for the growth of many cancers such as non-small cell lung cancer (NSCLC) (Qian et al., 2015) and prostate cancer (Cao et al., 2019). It has been reported that FXR1 binds to AU-rich elements (AREs) within the 3' untranslated region (3'UTR) and enhances the stability of tumor necrosis factor alpha (*TNF- $\alpha$* ) and *COX2* mRNAs (Li et al., 2018; Vasudevan and Steitz, 2007). The conserved nucleotide sequence motif in AREs is AUUUA, which occurs in variable length repetitions in the 3'UTR of mRNAs (Glisovic et al., 2008). However, it is unclear how FXR1 stabilizes its target mRNAs and promotes their translation and whether it is important for the pathophysiology and progression of ovarian cancer. In this paper, we describe how FXR1 binds to the ARE within *cMYC* mRNA, enhancing its translation to cMYC oncoprotein and a multifunctional transcription factor, which is important for the growth and aggressiveness of ovarian cancer.

## RESULTS

### FXR1 CNV associates with high expression of FXR1 and poor cancer outcomes

To identify the genes within the 3q26 locus that contribute to ovarian cancer oncogenesis, we used the high-resolution SNP-based copy number analysis of 579 patients with HGSOC in the TCGA datasets. Interestingly, our analysis revealed that FXR1 is highly amplified or copy-number gained in >40% patients of HGSOC (Figure 1A). To investigate whether FXR1's expression profile is also altered in other cancers due to CNV, we interrogated the TCGA dataset in cBioPortal (<https://www.cbioportal.org/>) and Clinical Proteomic Tumor Analysis Consortium (CPTAC) for CNV, gene expression, and protein changes. We also employed the UALCAN (<http://ualcan.path.uab.edu/>) portal for determining alterations in FXR1 expression in various human cancers and found that FXR1 is frequently amplified

in lung, ovarian, cervical, colon, and breast cancers (Figures 1B and S1A). Notably, FXR1 CNVs were found to be associated with increased expression and levels of both *FXR1* mRNA and FXR1 protein in patients with ovarian cancer in the TCGA dataset (Figure 1C). Similarly, FXR1 CNV associated with *FXR1* mRNA in patients with breast cancer, lung adenocarcinoma (LUAD), and lung squamous carcinoma (LUSC) in the TCGA dataset (Figure S1B). Moreover, FXR1 protein levels are markedly increased in advanced ovarian tumors and are highly expressed in high grade ovarian cancer (Figure S1C). Together, our data suggest that a gain in the copy number or amplification of the FXR1 gene leads to an increase in the expression of *FXR1* mRNA and subsequently the high-level FXR1 protein. Our clinical outcome analysis based on *FXR1* mRNA in a publicly available ovarian cancer dataset (Tothill et al., 2008) demonstrated that high *FXR1* mRNA expression was associated with worse overall and recurrence-free survival in those patients (Figure 1D).

Next, we employed the gene set enrichment analysis (GSEA) to identify potential functional gene sets that are associated with high expression of FXR1. First, we ranked all the protein-coding genes based on their correlation with FXR1 expression. Then, we focused on functional gene sets related to cancer hall-marks. Here, we found that high expression of FXR1 showed the greatest association with two enrichment annotations that included MYC targets and E2F1 targets in TCGA ovarian, breast, LUAD, and LUSC datasets (Figures 1E and S1D). Our immunohistochemical (IHC) analysis to quantitate FXR1 protein using three tissue microarrays (TMAs) containing 212 ovarian cancer samples, 20 adjacent normal tissues, and 14 normal tissues (Figure S1E; Tables S1, S2, and S3) also displayed that metastatic samples expressed ~3-fold higher levels of FXR1 protein compared to normal and benign tissues. We also observed that the metastatic tissues exhibited the highest levels of FXR1 protein among all other groups (Figure 1F).

We then compared the levels of FXR1 protein in fresh ovarian cancer specimens and normal ovarian surface epithelium specimens. In line with our results above, we observed that FXR1 is markedly increased in ovarian cancer tissues compared to normal ovarian tissues (Figure 1G). Next, we compared the protein levels of FXR1 in normal fallopian surface-, ovarian surface-, and fallopian tube-derived epithelial cells with ovarian cancer cells and found that FXR1 is highly expressed in all the ovarian cancer cells compared to the normal ovarian surface and fallopian tube epithelial cells (Figure S1F). Taken together, our data demonstrated that FXR1 is highly expressed in patients with ovarian cancer primarily due to copy number gain or amplification.

### **Depletion of FXR1 reduces oncogenic properties of ovarian cancer cells**

Next, we determined the role of FXR1 on oncogenic characteristics in ovarian cancer cells and found that the knockdown of FXR1 impaired the growth and colony formation of ovarian cancer cells (Figures 2A–2C). Loss of FXR1 also reduced the invasiveness of ovarian cancer cells when cancer cells were seeded on Matrigel-coated trans-well inserts (Figure 2D). Next, we used a qPCR array to identify if FXR1 associated with the genes that regulate cell-cycle regulation, cell survival, and proliferation (Table S4). Importantly, the knockdown of FXR1 reduced the expression of *CDK4*, *CCNE1*, *CCND1*, *CDK2*, *CDK1*, and *CDK6*, whereas it upregulated the expression of cyclin-dependent kinase (CDK)

inhibitors such as *CDKN2A* and *CDKN1B* in HeyA8 ovarian cancer cells (Figure 2E). Our cell-cycle analysis demonstrated that the loss of FXR1 increased the number of cells in the G0/G1 phase with a concomitant decrease in the number of cells in the S and G2/M phases (Figure 2F). To corroborate these effects, we determined levels of cyclins and CDKs, which are important for the G1 growth phase and found that knockdown of FXR1 reduced levels of cyclin D1, cyclin E1, CDK4, CDK6, CDK2, and enhanced levels of CDKN2A (p16INK4A/MTS1) and CDKN2B (p15INK4B/MTS2) (Figure 2G).

Consistent with the changes in the levels of cell-cycle-associated proteins, we also observed morphological changes associated with cell death such as nuclear condensation and DNA fragmentation when FXR1 was knocked down in ovarian cancer cells (Figure S2A). Further, we investigated the effects of FXR1 knockdown on apoptosis by annexin V-FITC staining followed by flow cytometry. Notably, depletion of FXR1 increased apoptosis of OVCAR5, HeyA8, and Kuramochi cells, which were marked as Q2 populations in Figures 2H and S2B. In agreement, our GSEA based on *FXR1* mRNA expression demonstrated an inverse correlation of FXR1-associated genes with the functional annotation mark apoptosis in the TCGA datasets (Figures 2I and S2C). In conjunction, our qPCR analysis also demonstrated that the loss of FXR1 decreased the expression of *BCL2L1*, *CDK2*, *CCNB1*, *RAD51*, *HMGA1*, and *MCM2* and upregulated the expression of *CDKN1A* and *CDKN1B*, which were identified as the key genes as part of the functional annotation apoptosis (Figure S2D). We also found that loss of FXR1 increased cleaved caspase-3 and caspase-7 activities, which are surrogates for apoptosis (Figure S2E).

To further determine changes in levels of proteins related to cell death, we performed a protein array for apoptotic markers identifying that FXR1 depletion increased the levels of pro-apoptotic proteins BAX, cytochrome-C, death receptors FADD, FAS, p21, p27, and phospho-p53 (S15) and decreased levels of pro-survival proteins such as HSP-60 and Survivin (Figure S2F). In agreement, immunoblot analysis also showed that FXR1 deficiency upregulated the levels of BAX, p27, and p21 and reduced the levels of BCL2 (Figure S2G). Together, our results demonstrate that FXR1 knockdown inhibits the cell growth, prevents cell-cycle progression, and activates cell death pathways in cancer cells.

### **FXR1 regulates the expression of cMYC in ovarian cancer cells**

Many RBPs were known to regulate the stability of mRNAs and modulate protein translation (Harvey et al., 2017). Therefore, we determined whether FXR1 contributes to either gene-specific or global level translation in ovarian cancer cells. Here, we performed a surface sensing of translation (SUnSET) assay, using puromycin antibiotic, a structural analog of aminoacyl tRNAs that mimics tyrosyl- or phenylalanyl-tRNA, binds in the ribosomal A-site, and is incorporated into nascent polypeptide chain during elongation (Figure S3A). In corollary, ribosome uses puromycin as a substrate during protein elongation step, where it forms a peptide bond with the p-site peptidyl-tRNA. This transpeptidation step results into the termination of polypeptide synthesis during peptide elongation and release of an abortive or truncated peptidyl-puromycin product from the ribosome (Schmidt et al., 2009) (Figures 3A and S3A).

We performed two independent experiments using the principle of SUNSET assay. First, we treated FXR1 knockdown cell with puromycin and performed immunoblot. We also fixed and permeabilized the above cells and immune-stained using fluorochrome-labeled anti-puromycin antibody and performed fluorescently activated cell sorting (FACS). In both assays, we found that the loss of FXR1 inhibited overall protein synthesis that was quantitated as the abundance of puromycin-incorporated peptides (Figures 3B and 3C). In a complementary approach, we overexpressed FXR1 in OVCAR3 cells that express low levels of FXR1 (Figure S1F) and treated with puromycin. Notably, we found that an increase in FXR1 improved the overall protein synthesis (Figure S3B).

Next, we used a reverse phase protein array (RPPA) to evaluate proteins associated with various signaling networks in cancer cells (Hennessy et al., 2010). Our RPPA assay using FXR1 knocked-down cells identified that 34 proteins were altered significantly ( $p < 0.05$ ) compared to the control siRNA-transfected cells (Table S5), where 12 proteins were upregulated and 22 proteins were downregulated upon FXR1 knockdown (Figures 3D and S3C). Consistent with our finding that FXR1 inhibited apoptosis and promoted oncogenesis, silencing of FXR1 reduced the levels of many oncogenic proteins including cMYC, EVI1, CHK1, FOXM1, cyclin B1, and CDC6. The loss of FXR1 also upregulated CDKN1A (p21), DUSP4, FAK1, and PAI1 proteins, which are mainly involved in the cell death mechanisms of cancer cells (Figure 3D). Our pathway analysis of differentially expressed proteins using Ingenuity pathway analysis (IPA) software (Ingenuity Systems) identified that cell death and cell survival, cellular development, cellular growth and proliferation, cell cycle, and cancer are the top five enriched pathway annotations (Figure S3D).

We further validated if FXR1 interacts directly with all the top proteins with a p value  $< 0.00015$  (Table S5), which we identified by RPPA by RNA immunoprecipitation (RIP) followed by qPCR in three ovarian cancer cell lines (OVCAR5, HeyA8, and Kuramochi) (Figures 3E and 3F). Here, we used *p21* as positive control based on previous studies (Majumder et al., 2016) and  $\beta$ -actin as a negative control. Our RIP specific to FXR1 demonstrated an increased in the enrichment of *cMYC* mRNA among all the top proteins with p value  $< 0.00015$  that were identified by RPPA (Figure 3F). Then, we performed STRING protein interaction network using the proteins with a p value  $< 0.00015$  and found that cMYC is the central protein that demonstrates high connectivity with all the proteins we identified (Figure 3G). We observed that the knockdown of FXR1 reduced cMYC protein in multiple ovarian cancer cell lines (Figure 3H).

We also observed that FXR1 overexpression upregulated CDK4, CDK6, and CDK2 and promoted the colony formation of ovarian cancer cells (Figures S3E and S3F). Importantly, our TMAs stained for FXR1 and cMYC demonstrated a significant correlation of FXR1 with cMYC protein in both benign ( $r = 0.7164$ ,  $p < 0.0001$ ) and malignant ( $r = 0.5008$ ,  $p < 0.0001$ ) tissues of ovary (Figures S1E, S3G, and S3H; Tables S1, S2, and S3). To further confirm that the effects of FXR1 mediated through cMYC, we rescued cMYC using cMYC CDS without 3'UTR in FXR1-depleted cells (Figure 3I) and found that the rescue of cMYC recovered the loss in colony formation and cellular invasion induced by FXR1 (Figure 3J). Taken together, our data demonstrate that cMYC is the key target of FXR1 for its oncogenic effects in ovarian cancer.

## Depletion of FXR1 suppresses the growth of ovarian cancer cells and improves the survival of mice bearing orthotopic ovarian tumors

Based on our *in vitro* data, we postulated that inhibiting the levels of FXR1 reduces tumor burden *in vivo*. To test this hypothesis, we stably knocked down FXR1 in HeyA8 cell line, using two different short hairpin RNAs (shRNA) (TRCN0000160812 labeled as shFXR1-1 and TRCN0000160901 labeled as shFXR1-2) or a nonspecific control shRNA (shCont) cloned in pLKO.1 vector. Of the two sequences, TRCN0000160901 (shFXR1-2) produced the greatest decrease in FXR1 levels (Figure 4A). Stably knocked down cells and control cells were selected after puromycin treatment (8  $\mu\text{g}/\text{mL}$ ), where we found that the level of FXR1 protein was markedly reduced in the shFXR1 cells compared with the shCont cells in all the clones (1–5) (Figure 4A). Consistent with our results in Figure 3, stable knockdown of FXR1 resulted into the decrease of cMYC expression markedly (Figure 4A). From these clones, we selected clone 1 for further functional assays. In agreement with our siRNA results in Figure 2, knocking down FXR1 also decreased cell proliferation and colony formation of HeyA8 cells (Figures 4B and 4C).

To determine the consequences of FXR1 loss *in vivo*, we injected the control cells or FXR1-knockdown HeyA8 cells into the ovary bursa of nude mice orthotopically and monitored tumor progression (n = 8 mice/group) for up to 5 weeks by bioluminescence *in vivo* imaging system (IVIS) (Figure 4D). Our analysis showed that FXR1 knockdown reduced ovarian tumor burden by ~70% at the last three time points (Figure 4E). We also found that silencing FXR1 had markedly reduced tumor growth at both the primary site of injection and metastatic abdominal sites at the endpoint (Figures 4F to 4H). We also monitored the effects of changes in tumor burden on survival until all the mice in the shFXR1 group (n = 10 mice/group) died (Figure 4I). Importantly, this analysis found that the mice injected with shFXR1-HeyA8 cells had survived longer than the shCont mice (median survival of 105 days versus 33 days, log-rank test  $p < 0.0001$ ) (Figure 4J). Our immunoblot analysis of the tumor lysates also showed that the tumors with stably knocked down FXR1 expressed lower levels of cMYC and cyclin D1 compared to the controls (Figure 4K). Conversely, those tumors expressed higher levels of p21 and p27 proteins (Figure 4K). Immunohistochemistry on tumor tissues collected from the mice also showed that depletion of FXR1 decreased the levels of pro-survival marker Ki67 and cMYC oncoprotein. Notably, stable knockdown of FXR1 increased the levels of cleaved caspase-3, a pro-apoptotic marker, compared to the control tumors (Figure 4L). Taken together, our results demonstrate that silencing FXR1 expression inhibits the growth and metastasis of HeyA8 ovarian cancer cells *in vivo*.

## Inducible expression of FXR1 increases levels of pro-oncogenic proteins and promotes oncogenic characteristics in ovarian cancer cells

Next, we created an efficient and controlled model for inducing FXR1 and monitoring tumor growth by using a tetracycline (tet)-inducible vector carries FXR1-fused GFP expressing HeyA8 ovarian cancer cells (Figure S4A). Cells that stably expressed inducible GFP-FXR1 were selected by FACS sorting after tetracycline treatment (1  $\mu\text{g}/\text{mL}$ ) (Figure S4A). As expected, induction of FXR1 promoted the proliferation and colony formation of ovarian cancer cells compared to their control groups (Figures S4B and S4C). Our data also

demonstrated that FXR1 induction by tetracycline increased the levels of cMYC, CDK2, CDK4, and CDK6 proteins (Figure S4D).

Then, we determined the effect of FXR1 on ovarian cancer progression *in vivo* by orthotopically injecting luciferase-tagged HeyA8 cells that stably expressed tet-inducible FXR1 into the left ovary bursa of (Foxn1/Nu) nude mice (n = 8/group) (Figure S4E). Mice were treated with doxycycline (Dox, which is the Dox-derivative of tetracycline) in their drinking water (2 mg/mL) throughout the experiment to maintain increased expression of FXR1. We then monitored tumor growth through bioluminescent imaging (Figure S4F). Induction of FXR1 by Dox promoted the growth of tumors from ovarian cancer cells at the primary injection site and increased the rate of metastasis to other ovary and other organ sites (Figures S4F–S4I; Videos S1 and S2). As expected, Dox-treated mice expressed high levels of FXR1 in their tumors along with increased levels of cMYC and cyclin D1 (Figure S4J). Those tumors also expressed high levels of the proliferative marker Ki67 and low levels of the apoptosis marker cleaved caspase-3 compared to the mice not treated with Dox (Figure S4K). Taken together, these results complemented our *in vitro* and *in vivo* data of silencing FXR1 reduced tumor cell growth both *in vitro* and *in vivo* (Figures 2 and 4) whereas its overexpression promoted tumor growth and metastasis *in vivo*.

### Binding of FXR1 onto cMYC mRNA improves stability and enhances cMYC translation

Next, we sought to decipher the molecular mechanism that enables FXR1 to regulate cMYC levels in ovarian cancer cells. First, we tested the effect of FXR1 on cMYC mRNA translation with an *in vitro* translation assay, using the rabbit reticulocyte lysate system. As shown in Figure 5A, the yield of cMYC protein increased more in HeyA8 cells in the presence of purified FXR1 protein. Second, we determined how FXR1 modulates cMYC protein level and its turnover rate. For this experiment, we transfected HeyA8 and Kuramochi cells with either control siRNAs or siRNAs specific to FXR1. The transfected cells were then treated with CHX for indicated time points, and cMYC protein levels were monitored. As shown in Figures 5B and S5A, inhibition of FXR1 resulted into rapid degradation of cMYC protein with ~50% reduction in half-life in both cell lines. In a complementary approach, we performed a CHX-chase experiment while inducing FXR1 expression in HeyA8 cells. As expected, overexpression of FXR1 in HeyA8 cells improved the stability of cMYC protein compared to the control (~68.5 min versus 48.2 min) (Figure S5B). Third, we determined whether FXR1 alterations make any attributable effects on cMYC transcript levels. Here, we pre-transfected the cells with siFXR1, then treated with actinomycin-D (Act D) for indicated time points in HeyA8 and Kuramochi cells and observed that silencing of FXR1 increased the rate of degradation of cMYC mRNA (~95 min) in HeyA8 cells compared to control (~150 min), and (~100 min) as compared with control (~160 min) in Kuramochi cells (Figure S5C). Conversely, FXR1 overexpression enhanced cMYC mRNA stability compared to the control (~169 min versus 118 min) (Figure S5D).

We then sought to determine how FXR1 enhances the translation of cMYC mRNA into protein. Translation initiation is the rate-limiting step of protein production, which begins with the loading of the 43S pre-initiation complex (43S PIC, 40S ribosomal

subunit associated with several initiation factors including a eIF2-GTP-Met-tRNA<sup>Met</sup> ternary complex) onto the 5' mRNA cap bound to an eIF4F complex (consisting of the cap-binding proteins eIF4E/eIF4G, the helicase eIF4A, and the poly(A)-binding protein) (de la Parra et al., 2018). To determine if FXR1 interacts with any eIF4F complex, we prepared the whole cell extracts of HeyA8 cells and immunoprecipitated FXR1, where we observed a strong interaction of FXR1 with both eIF4A1 and eIF4E proteins (Figure 5C). In a complimentary approach, we immunoprecipitated eIF4A1 and eIF4E, showing that eIF4A1 and eIF4E interact with FXR1 (Figure 5C). Consistent with these observations, our immunofluorescence assay showed co-localization of FXR1 with eIF4A1, eIF4E, or eIF4G1 in ovarian cancer cells (Figure S5E). Collectively, these data suggest a strong association of FXR1 with proteins in the eIF4F complex. In conjunction, we also found that the levels of FXR1 protein correlated directly with eIF4F family proteins in patients with ovarian cancer (Figure S5F). Again, these findings supported the notion that FXR1 is an important regulator of translation initiation. Compatible with our data that FXR1 associates with eIF4F complex proteins, we postulated that FXR1 facilitates the assembly of the translation initiation complex on the mRNA cap to promote protein synthesis. To confirm this concept, we performed m<sup>7</sup>GTP (5' mRNA cap analog) cap pull-down assay in FXR1-depleted cells followed by immunoblotting of m<sup>7</sup>G cap interacting proteins (Figure 5D) and found that the loss of FXR1 reduced the interaction of eIF4A1, eIF4E, and eIF4G1 with m<sup>7</sup>G cap analog (Figure 5D).

We next attempted to identify the specific domain in FXR1, which is required for its interaction with eIF4F complex proteins. FXR1 contains multiple functional domains including N-terminal tandem Tudor domains (Tud1 and Tud2), K homology (KH) domain, and the C-terminal region arginine-glycine-glycine repeat (RGG) box domain, as illustrated in Figure 5E. To determine which domain in FXR1 is precisely required for its interactions with eIF4F proteins, we transfected pLCP vector expressing wild-type (WT) full-length FXR1 (FXR1<sup>FL</sup>), deletion of either Tudor domain 1 or Tudor domain 2 (FXR1<sup>Tud1</sup> or FXR1<sup>Tud2</sup>), deletion of RGG-box (FXR1<sup>RGG</sup>), or deletion of C-terminal portion (FXR1<sup>C</sup>) fused with RFP (Figure 5E) and immunoprecipitated RFP TRAP-coated beads (Figure S5G). In this assay, we found that the deletion of RGG motif abolished the interaction of FXR1 with eIF4A1, eIF4E, and eIF4G1 proteins (Figure 5F). Notably, we found that cMYC level is increased upon the transfection of all the constructs express FXR1 except RGG mutant FXR1 (FXR1<sup>RGG</sup>) (Figure 5G). Taken together, our results demonstrate that RGG-box domain in FXR1 is required for the recruitment eIF4F complex to the translation initiation site of mRNA.

Based on our data that demonstrate FXR1 promotes cMYC translation, we sought to determine the translational efficiency regulated by FXR1. To this end, we knocked down FXR1 in HeyA8 cells and prepared cytoplasmic fractions, which were further fractionated on 5%–50% linear sucrose gradient columns (Figure 5H). By recording absorbance of the fractions at 254 nm to profile polysome content, we obtained four peaks representing 40S and 60S ribosomal subunits, 80S monosomes and polysomes (left to right, Figure 5I). Notably, this assay showed a lower polysomal mRNA peak, which is the marker of active translation when FXR1 was knocked down compared to its control. In contrast, monosomal peaks (80S) increased, which indicated inefficient translation or translational repression due

to loss of FXR1 expression (Figure 5I). We also loaded the gradient fractions onto SDS-PAGE, performed western blot analysis, and found that knocking down of FXR1 caused a striking reduction in the level of ribosomal protein RPS6 (S6) compared to the control due to the deficiency of polysomes in the associated fractions (Figure 5J). Next, we quantitated the levels of *cMYC* mRNA in the polysome fractions by qPCR using the mRNA purified from the ribosomal fractions. In agreement with our data that FXR1 promotes *cMYC* translation, we observed a reduction in the expression of *cMYC* mRNA in polysome fractions, when FXR1 was depleted (Figure 5K). Of note, we did not find any change in  $\beta$ -actin mRNA in polysome fractions that we employed as a negative control (Figure S5H). In sum, our results demonstrate that binding of FXR1 onto *cMYC* mRNA enhances translation by recruiting eIF4F complex to the translation initiation site on *cMYC* mRNA.

### **FXR1 directly interacts with AU-rich elements in the 3'UTR of *cMYC* for protein translation**

Next, we sought to determine if FXR1 could bind to AREs within the 3'UTR of *cMYC* mRNA to promote post-transcriptional changes. For this, we synthesized biotinylated RNA probes containing all six AREs spanning the entire *cMYC* 3'UTR (ARE1, ARE2, ARE3, ARE4, ARE5, and ARE6) and then performed RNA electrophoretic mobility shift assays (REMSA) (Figure 6A and 6B; Table S6). We used two random probes that lack ARE sequences, R1 and R2 as negative controls (Table S6). The probes encompassing ARE1, ARE2, ARE4, and ARE5 showed strong binding with recombinant FXR1-GST protein but not with control GST protein, whereas the other two probe targets exhibited weak (ARE3) or poor (ARE6) affinity with FXR1. Notably, the incubation of samples with excess amounts of cold probes decreased the binding of FXR1 with ARE further confirmed the specificity of the interaction of our probes with ARE sequences (Figures 6C and S6A). As expected, no interactions were observed between the nonspecific R1 and R2 probes when incubated with FXR1 protein (Figure S6B).

To provide additional evidence that FXR1 binds with AREs within the 3'UTR of *cMYC* mRNA, we transfected the FAM fluorochrome-labeled oligonucleotides spanning the entire *cMYC* 3'UTR in the HeyA8 and Kuramochi cells (Table S7) and performed an RNA-proximity ligation assay (RNA-PLA), which detected close proximity between FXR1 protein likewise the ARE probes we identified in our REMSA (Figure 6D). In this assay, we used five biotin-labeled PLA probes (probe 1 to probe 5) that are 7 bases away from each ARE and one random probe (probe 6) that lacks ARE sequence as a negative control (Figure S6C; Table S8). PLA signals generated upon the interaction of FXR1-targeting antibody and biotin-tagged antibody that bind to the biotinylated ARE-specific probe were monitored (Figure 6E). In complement to our REMSA results, the PLA probe-1 (close to ARE1 and ARE2) and the PLA probe-3 (close to ARE4) provided highest fluorescent signals of proximity. PLA probes 2 and 4 (respectively close to ARE3 and ARE5) yielded moderate signals; whereas PLA probe 5 (close to ARE6) gave only weak signals in both HeyA8 and Kuramochi cell lines (Figures 6E and S6D). Notably, PLA probe 6, which is not proximal to any ARE, did not give any signal of interactions between connector oligos due to lack of proximal interactions (Figures 6E and S6D). To further confirm the signaling specificity due to FXR1 binding, we knocked down FXR1 using target-specific siRNAs. As expected, FXR1 knockdown resulted in a loss of proximity signal compared to the cells transfected

with control siRNA, even when we targeted their AREs using PLA probe 1, which had given the highest yield for proximal ligation (Figure S6E). Taken together, our results demonstrate that FXR1 binds to target-specific sequences within the 3'UTR of *cMYC* transcripts.

To further confirm that FXR1 binds to the 3' UTR of *cMYC* mRNA precisely in the ARE sequences, we performed a luciferase reporter assay, using a construct of wild-type 3'UTR of *cMYC* (FL*cMYC*-3'UTR-Luc) containing all the ARE sequences cloned in downstream of a dual (firefly and Renilla) luciferase (Luc) vector. We also used 3'UTR mutants (Mut1 to Mut4 indicates base substitution mutations in each site, as indicated) as controls (Figure 6F; Table S9). In this assay, we transiently transfected WT full-length 3'UTRs of the *cMYC* mRNA and four mutants (Mut1 to Mut4) into OVCAR3 cells that exogenously overexpressed FXR1 and quantified *cMYC* 3'UTR reporter signals (Figure 6G). As expected, overexpression of FXR1 along with FL-*cMYC*-3'UTRs increased luciferase reporter activity as compared to the empty control vector, whereas the mutations in the ARE sequences in the 3'UTR reduced luciferase reporter activity compared to the FL-*cMYC*-3'UTR (Figure 6G). Moreover, there was lower luciferase reporter activity in the mutants that were transiently transfected with control vector (Mut1 to Mut4) than in those that overexpressed FXR1 (Mut1 to Mut4) (Figure 6G). These results demonstrate that FXR1 binds to the FL-*cMYC*-3' UTR of *cMYC* transcripts, increasing protein translation.

Next, we deleted AREs in the 3'UTR region of *cMYC* genome using CRISPR/CAS9 vectors and confirmed that 3'UTR region of *cMYC* is required for the effects of FXR1 in cancer cells (Figures S7A–S7C) and overexpressed FXR1 in the WT OVCAR3 cells and in the cells where AREs-deleted in *cMYC* 3'UTR in the presence or absence of *cMYC*-gene with native 3'UTR. This assay confirmed that overexpression of FXR1 did not affect the *cMYC* level and the colony-forming ability of the ARE-deleted cells. In contrast, FXR1 overexpression improved the *cMYC* level and colony-forming ability of cells when rescued the *cMYC* by introducing *cMYC* gene with its native 3'UTR (Figures S7D and S7E). We also observed that ARE deletion in *cMYC* 3'UTR resulted into a rapid degradation of *cMYC* mRNA compared to the WT at baseline, whereas FXR1 depletion did not make any marked change in *cMYC* mRNA stability in the cells where AREs were deleted in *cMYC* 3'UTR (Figures S7F and S7G).

Together, our results suggest that FXR1 binds onto the target-specific AREs located within 3'UTR of *cMYC* and stabilizes *cMYC* mRNA. FXR1 binding also facilitates the recruitment and assembly of eukaryotic initiation factors (eIFs) to the translation initiation site and promotes mRNA circularization potentially for a swift recycle or transfer of ribosomes from 3'UTR sites to the translation initiation site (Figure 6H). Consequently, these events improve the translation of *cMYC* mRNA and further boost the oncogenicity of cancer cells for increased tumor growth and metastasis.

### ***In vivo* delivery of FXR1 siRNA incorporated in DOPC liposome inhibited the growth and metastasis of ovarian cancer in orthotopic model of ovarian cancer**

Next, we sought to determine the potential of inhibiting FXR1 therapeutically. For this aim, we delivered siRNA of FXR1 (siFXR1) *in vivo* in the mice bearing ovarian cancer cells. First, we determined the localization of siFXR1 in ovarian cancer cells and

subsequent cell death, and then followed by assessing stability of naked siFXR1 versus siFXR1 incorporated in neutral 1,2-dioleoyl-sn-glycero-3 phosphatidylcholine (DOPC) nanoliposomes for therapeutic use. As expected, siFXR1 RNA was easily incorporated in ovarian cancer cells (red fluorescence) and its incorporation induced cell death of ovarian cancer cells (green fluorescence) (Figure 7A). Importantly, we observed that the DOPC incorporation improved the stability of siFXR1 when we incubated with serum at 37°C, whereas the naked siRNA was easily degraded to smaller fragments over indicated time points (Figure 7B). Thus, we determined the effect of FXR1 siRNA encapsulated nanoliposomes on ovarian cancer growth and progression *in vivo* and found that the delivery of siFXR1 reduced the overall tumor growth in both primary sites of injection as well as in peritoneal organs (Figures 7C–7G). Delivery of siFXR1 also improved the survival of mice bearing ovarian cancer compared to the mice that were treated with control siRNA (Figures 7H and 7I). In conjunction, treatment with siFXR1 reduced the expression of cellular proliferation marker Ki67 and cMYC, which is the key target of FXR1. Delivery of siFXR1 also upregulated the levels of apoptotic marker cleaved caspase-3 and cyclin-dependent kinase inhibitors p21 and p27 in tumor tissues (Figures 7J and 7K). Together, our results demonstrated that knocking down of FXR1 using therapeutic approach was effective in inhibiting the growth and metastasis of ovarian cancer.

## DISCUSSION

RBP are known for post-transcriptional actions that regulate the expression of many genes, including proto-oncogenes, apoptosis regulators, cell-cycle associated genes, and pro-inflammatory cytokines. These actions are regulated mainly by changing the decay kinetics of target mRNAs or altering translation of several genes often associated with pathobiological functions (Cao et al., 2019). We report that a large subset of patients with ovarian cancer expresses high levels of FXR1 due to CNV. Such patients suffered poor clinical outcomes compared with patients with low FXR1 levels, suggesting that FXR1 is an important oncoprotein has critical roles in the pathophysiology of ovarian cancer.

By analyzing the TCGA and other publicly available ovarian cancer databases, we demonstrated that FXR1 high expression directly correlated with tumor grades and stages and was associated with poor survival. Congruently, a recent study demonstrated that FXR1 promotes prostate cancer progression by directly associating with *FBXO4* 3' UTR and thereby upregulating mRNA stability (Cao et al., 2019). FXR1 expression was also reported to be upregulated in NCSLC, prostate, glioblastoma, and ovarian cancer (Sekulovski et al., 2021; Truitt and Ruggero, 2016). However, its key targets and its mechanism of actions were not well studied for ovarian cancer. We have identified that cMYC is the key target of FXR1 in ovarian cancer. Our study further corroborated that FXR1 is crucial for the survival and proliferation of ovarian cancer cells both *in vitro* and *in vivo*. Therefore, targeting FXR1 therapeutically might represent a promising strategy for the treatment of ovarian cancer.

Our RIP and RPPA demonstrated that cMYC was decreased and p21 was increased when FXR1 was knocked down in ovarian cancer. Indeed, we found that many candidate genes were the potential direct or indirect target of FXR1 and these candidates were also involved in the progression and metastasis of ovarian cancer. We also found that FXR1 promoted

the overall translation in cancer cells, which is a critical feature for oncogenesis. Previous studies have demonstrated a possible mechanism of how FXR1 regulates p21 by binding the G-quadruplex (G4) RNA structure within the mRNA encoding p21 (cyclin-dependent kinase inhibitor 1A [CDKN1A], Cip1) gene (Gabay et al., 2014; Li et al., 2014), whereas the precise mechanism that promoted by FXR1 was not well understood. We found that FXR1-mediated cMYC upregulation promoted the levels of cell-cycle regulators including cyclin E1, cyclin D1, and CDKs for ovarian cancer growth progression. We proved that the oncogenic actions including cell proliferation and metastatic features induced by FXR1 were mediated through cMYC protein in ovarian cancer cells. cMYC oncogene is one of the commonly upregulated oncogenes in human cancers, being dysregulated in more than 40% of cases, and its high expression is frequently associated with poor prognosis and unfavorable patient survival (Baker et al., 1990; Jung et al., 2018).

Our mechanistic investigation provided evidence that FXR1 upregulated cMYC protein levels by stabilizing *cMYC* mRNA via binding to specific sequences of ARE (AUUUA) within its 3'UTR, and the binding of FXR1 onto *cMYC* mRNA improved cMYC translation. It was reported that FXR1 acted as a translation activator and showed interaction with the 60S ribosomal subunit (Ruggero, 2013). In conjunction, we observed that FXR1 improved the stability of *cMYC* mRNA and promoted the enrichment of polysomes on *cMYC* mRNA which is a known mechanism for protein translation. Using CRISPR/Cas9-mediated deletions of ARE sequences in the 3'UTR of cMYC gene, we confirmed that the ARE sequences in cMYC are important for the oncogenic actions of FXR1.

Our immunoprecipitation and co-localization assays verified that FXR1 recruits eIFs to the translation initiation site. We also showed that the interaction between the RGG domain in FXR1 is required for its interaction with eIF4A1, eIF4E, and eIF4G1 for cMYC translation. The interaction between eIF4F proteins and the 7-methylguanosine “cap” (m<sup>7</sup>G) located at the 5' end of all mRNAs is critical to directly recruit the 40S ribosomal subunit to mRNAs through a set of protein-protein interactions and to unwind RNA secondary structures in the 5' untranslated region (5'UTR) of mRNAs (Borman et al., 2002). Our data suggest that the FXR1-eIF4F loop promotes translation, presumably by recycling ribosomes as proposed for eIF4G-PABPC1-mediated mRNA looping, which was established previously (Fatscher et al., 2014). Supporting this notion, looping between the stop codon and the 5'UTR end might be a more efficient way to recycle or transfer ribosomes rather than via the 3'UTR end, especially for mRNAs with long 3'UTRs, because ribosomes would dissociate from the mRNP once ribosomes were released at the stop codon. Taken together, our data suggest a potential mechanism of action of how FXR1 that facilitates the looping of mRNA for circularization through its interaction with cMYC 3'UTR and eIF4 family proteins (Figure 6H).

Direct targeting of cMYC has been a challenge for decades owing to its “undruggable” protein structure. Thus, FXR1 may represent a target that holds great potential for suppressing cMYC expression in ovarian and other cancers. In our therapeutic approaches, we found that inhibiting FXR1 using siRNAs specific to FXR1 incorporated in DOPC nanoliposomes inhibited ovarian cancer growth and metastasis. FXR1 is highly amplified and expressed in many human cancers including lung, cervical, head, and neck carcinomas.

Therefore, the mechanism we identified and the therapeutic approaches of inhibiting FXR1 could be broadly applicable to other cancers that encompass FXR1 CNV. It is also highly possible that FXR1 can directly regulate many other mRNAs as its targets, which could be further elucidated using an unbiased genome-wide analysis instead of a medium throughput assay. Such studies of identifying all potential targets of FXR1, as well as testing the potential of inhibiting FXR1 for cancer therapy, are currently ongoing in our laboratory.

## STAR★METHODS

### RESOURCE AVAILABILITY

**Lead contact**—Further information and requests for resources and reagents should be directed to and will be fulfilled by the lead contact, Pradeep Chaluvally-Raghavan (pchaluvally@mcw.edu).

**Materials availability**—This study did not generate new unique reagents.

#### Data and code availability

- The authors declare that all data supporting the findings of this study are available within the paper and its supporting information files and accession numbers or DOIs are listed in the key resources table are publicly available as of the date of publication.
- This paper does not report any original code.
- Any additional information required to reanalyze the data reported in this paper is available from the lead contact upon request. Raw data of western blots can be found at Mendeley Data, V1, <https://doi.org/10.17632/mgb7tv29jn.1> and raw data of reverse phase protein array can be found at Mendeley Data, <https://doi.org/10.17632/jn296wnwff.1>

### EXPERIMENTAL MODEL AND SUBJECT DETAILS

**Patient Samples**—After informed consent, normal ovarian epithelial tissues and serous epithelial ovarian cancer tissues were collected from female ovarian cancer patients according to an Institutional Review Board approved protocol at Medical College of Wisconsin. Normal ovarian tissues were collected from the tumor-free ovary of female patients with unilateral ovarian cancer or female patients with other gynecological cancers not involving the ovary. Ovarian cancer is the disease of females and all the clinical samples we used and the primary cell lines we developed are from females between the age of 30 and 70 years.

**Cell culture**—OVCAR3, SKOV3, OVCAR5, OVCAR8, and A2780 were purchased from the National Cancer Institute (NCI) cell line repository. HeyA8 cells were received from the Characterized Cell Line core at MD Anderson Cancer Center, Houston, TX, USA. PEO1 cells were received from Daniela E Matei, Northwestern University, Chicago, Illinois, USA. Kuramochi cells were received from Taru Muranen at Beth Israel Deaconess Medical Center, Boston, Massachusetts, USA. Immortalized fallopian tube epithelial cells FTE188

was received from Jinsong Liu and MCAS was received from Gordon Mills at MD Anderson Cancer Center, Houston, Texas, USA. All cancer cell lines were cultured in RPMI medium (Sigma-Aldrich, Saint Louis, MO) supplemented with 10% fetal bovine serum (FBS, Atlanta Biologicals, GA, USA), penicillin (100 U/ml) and streptomycin (0.1 µg/ml) and Sodium pyruvate (Sigma-Aldrich). FTE188 was maintained in cell culture medium consisting of 1:1 Medium 199 and MCDB105 medium (Sigma-Aldrich) with 10% FBS and 10ng/ml EGF (Sigma-Aldrich). Primary normal human OSE and FTE cells were cultured in MCDB105/199 (1:1)/15% fetal bovine serum/epidermal growth factor (10 ng/mL)/hydrocortisone (0.5 µg/mL)/insulin (5 µg/mL)/bovine pituitary extract (34 µg protein/mL). Cells were routinely tested and deemed free of Plasmotest™ Mycoplasma Detection Kit (InvivoGen, San Diego, CA). Authenticity of the cell lines used were confirmed by STR characterization at IDEXX Bioanalytics Services (Columbia, MO).

## METHOD DETAILS

**Tumor models and Animal Experiments**—All animal experiments were conducted under the institutional guidelines and were approved by Institutional Animal Care and Use Committee (IACUC) at the Medical College of Wisconsin. Female athymic nude mice (CrTac: NCr-Foxn1nu, Taconic Laboratories, RRID: IMSR\_TAC:ncnu), approximately 4 to 6 weeks old were maintained under specific pathogen-free conditions in accordance with guidelines and therapeutic interventions approved by the Institutional Animal Care and Use Committee. For tumorigenicity study, HeyA8 cells with stable knockdown of FXR1 (shFXR1) and control cells (shCont) were trypsinized, washed and resuspended in Hanks' balanced salt solution (GIBCO, Carlsbad, CA), then a total number of 25,000 cells/mice in culture medium were injected orthotopically into the ovarian bursa of the anesthetized female nude mice (n = 8) through a 1.5 cm intraperitoneal incision as described before (Pradeep et al., 2014). For survival study, shCont and shFXR1 cells were injected intraperitoneally in mice (n = 10). Similarly, HeyA8 cells with stable Tet-induced FXR1 overexpressed (Tet (+)) and control (Tet (-)) cells were processed and injected into mice ovary orthotopically (n = 8) followed by Doxycycline (2mg/ml) and 10% (w/v) sucrose (Sigma-Aldrich) in drinking water after 1 weeks of cells inoculation. The solution was protected was freshly prepared every second day. Tumor tissue was prepared as snap frozen for protein isolation or fixed in 10% formalin for immunohistochemistry.

siRNAs (siCont and siFXR1) for *in vivo* delivery incorporated into DOPC-nanliposomes were synthesized at MD Anderson Cancer Center (Landen et al., 2005). For therapy study, Luciferase tagged HeyA8 cells were processed and injected into mice ovary orthotopically (n = 8) and liposomal siRNA (5 µg) was given as a 200 mL intraperitoneally twice a week starting 1 week after inoculation cancer cells. For survival study, HeyA8 cells were injected intraperitoneally in mice (n = 10) and likewise DOPC-siRNA was given twice a week intraperitoneally.

**Serum stability assay**—Naked siFXR1 and siFXR1 incorporated DOPC (10 µmol/L) were incubated at 37°C in 10% fetal bovine (Invitrogen) or mouse serum diluted in PBS. Aliquots of 5 µl were withdrawn at different time points and immediately frozen in TBE-loading buffer. Samples were subjected to electrophoresis in 20% polyacrylamide–TBE

under non-denaturing conditions and visualized by staining with ethidium bromide and quantified by ImageJ software.

**Tissue Micro-Array (TMA) and immunohistochemistry (IHC)**—FXR1 and cMYC protein levels in human ovarian cancer tissues were analyzed using three TMAs (Cat# OV1005bt, Cat# OVC961 and Cat#OV1004, US Biomax Inc., Rockville, MD). For this purpose, the slides were dewaxed in xylene, and rehydrated through graded ethanol to distilled water. Antigen retrieval for the slide specimens were performed using IHC-Tek epitope retrieval solution and steamer set (IHC World, LLC.). The slides were then immersed in 3% H<sub>2</sub>O<sub>2</sub> for 10 min to quench endogenous peroxidase followed by blocking with 10% goat serum for 1 h. Vectastain ABC-AP Kit (Vector Labs, Burlingame, CA) and Vector Red Alkaline Phosphatase Substrate Kit I (Vector Labs, Burlingame, CA) were used for tissue staining as per manufacture protocol. FXR1 primary antibody (Proteintech, Cat#13194-1-AP) was used at 1:200 dilution and cMYC primary antibody (Santacruz Biotechnology, Cat#sc-47694) at 1:100. Following, Vector red staining, the slides were counterstained with Harris modified hematoxylin (Thermo Fisher Scientific Inc., Rockford, IL), dehydrated with graded ethanol and xylene, and finally mounted with paramount. TMAs slides was digitally scanned using Panoramic 250 FLASH III scanner (3D HISTECH ltd. Version 2.0) and, using the Case Viewer software (3D HISTECH ltd. Version 2.0) was used to view and analyze images.

**Western blotting**—For preparing cell lysates, the cells were washed twice with ice-cold PBS and lysed on ice in 1x RIPA lysis buffer containing freshly added protease inhibitor cocktails (Thermo Fisher Scientific Inc., Rockford, IL, USA) and 1 mM PMSF. For preparing the tissue lysates, the tumor tissues were homogenized in 1x RIPA lysis buffer over ice. After 30 min of incubation, the lysates were collected by centrifugation at 4°C for 10 min at 10,000 rpm. The amount of total protein was determined using a BCA protein assay kit (Pierce, Rockford, IL, USA). An equal amount of total protein (30 µg) was resolved on precast 4%–12% SDS-PAGE gels (Biorad, Hercules, CA, USA), transferred onto PVDF membranes, and incubated with desired primary antibodies, followed washing and incubation with HRP conjugated secondary antibodies and detecting of protein bands using chemiluminescence kit (Pierce, Rockford, IL, USA).

**siRNA transfection**—Predesigned siRNAs for human FXR1 were purchased from Thermo Fisher Scientific Inc., Waltham, MA and negative siRNAs universal control (siCont) from Sigma-Aldrich. Reverse transfections were performed using the Lipofectamine RNAiMAX transfection reagent (Thermo Fisher Scientific Inc., Waltham, MA). At 48 h post-transfection, cells were harvested for further analysis. siRNA sequences are listed below:

FXR1 siRNA (siFXR1-1):

Sense: GGAAUGACUGAAUCUGAUAtt

Antisense: UAUCAGAUUCAGUCAUUCat

FXR1 siRNA (siFXR1-2):

Sense: CGAGCUGAGUGAUUGGUCAtt

Antisense: UGACCAAUCACUCAGCUCGtc

**Cell proliferation, colony formation and cell invasion assays**—Cell viability was measured with the Cell Counting Kit-8 (CCK-8) (Dojindo, Shanghai, China) according to the manufacturer's instructions. Cells were plated at a density of  $1 \times 10^3$  cells per well in 96-well plates and incubated at 37°C. Proliferation rates were determined at 24, 48, 72 h post-transfection, and quantification was performed on a microtiter plate reader (Tecan, Mannedorf, Switzerland) at 450nm.

For colony formation assay, transfected cells were plated in six-well plates at a density of 1000 cells per well. After 10 days, cells were rinsed with PBS, fixed in 5% glutaraldehyde for 10min and then stained with 0.5% crystal violet (Sigma Aldrich, MO, USA) for 20min. Plates were washed with water and dried before imaging.

Ovarian cancer cells were treated with siCont and siFXR1s for 12h followed by re-plating of treated cells ( $2 \times 10^5$  cells) to the matrigel (Corning NY, USA) coated inserts in the presence of cell cycle inhibitors mitomycin C (5 µg/ml). Cells were incubated at 37°C for 24h for invasion assays. Cells that did not invade through the pores were removed using a cotton swab and inserts were washed and stained with 0.5% crystal violet for imaging. Alternatively, stained membranes were dissolved in 10% acetic acid, and quantified in microplate reader (Tecan, Mannedorf, Switzerland) at 560 nm.

**Quantitative real time-PCR (qRT-PCR)**—Total RNA was isolated from the cells using RNeasy Mini Kit (QIAGEN, Valencia, CA, USA) and first strand cDNA was transcribed with Oligo(dT) primers, dNTPs and M-MLV reverse transcriptase (Promega, Fitchburg, WI, USA). qRT-PCR was performed using CFX Connect Real-Time PCR systems (Biorad, Hercules, CA, USA) and SYBR Premix Ex TaqII (Biorad, Hercules, CA, USA) with first strand cDNA, forward and reverse primers. The list of primers is given in Table S10. The PCR program used was as follows, initial denaturation step (95°C for 30 s) followed by DNA amplification (95°C for 3 s followed by 60°C for 30 s) for 40 cycle. Melt curve analysis was performed to ensure the specificity of target amplicon. Relative mRNAs were analyzed using *GAPDH* as endogenous control and  $\Delta\Delta$ CT algorithm.

PCR array for human cell cycle (Cat#PAHS-020Z) and oncogenes and tumor suppressor genes (Cat#PAHS-502Z) was purchased from QIAGEN (Valencia, CA, USA), and was used according to the manufacturer's instructions. Data for PCR array were analyzed using RT<sup>2</sup> Profiler PCR Data Analysis software <https://geneglobe.qiagen.com/us/analyze>. Genes exhibit 1.5-fold-change in both directions with  $p < 0.05$  were considered significant. Five housekeeping genes, *B2M*, *HPRT1*, *RPLP0*, *GAPDH*, and *ACTB*, were used for normalizing data and fold change was calculated relative to the control siRNA group.

**Cell cycle analysis**—siFXR1s transfected ovarian cancer (OVCAR5, HeyA8 and Kuramochi) cells were seeded at a density of  $5 \times 10^5$  in 6-well plates. When cells reached 70%–80% confluence, they were washed with PBS, trypsinized, collected and fixed with 70% ethanol overnight. Next day, cells were treated with 1 µg/ml RNase A (Sigma-Aldrich,

Saint Louis, MO) at 37°C for 30 min and then resuspended in 0.5 mL of PBS and stained with 50 µg/ml propidium iodide (PI) (Sigma-Aldrich, Saint Louis, MO). The cells were analyzed using a FACScan flow cytometer (Becton–Dickinson, Mansfield, MA) and ModFit LT software (Verity Software, Topsham, ME).

**Live/dead cell assay**—Cellular death was measured with Live-or-Dye 488/515 Fixable Staining Kit (Biotium, USA) as per as manufacturer’s protocol. In brief, OVCAR5, HeyA8 and Kuramochi cells were reverse transfected with siRNAs (siCont and siFXR1). After 48h, the cells were washed with PBS and dye was added to the cells followed by incubation for 30min. Cells were fixed in 4% PFA, permeabilized with 0.5% Triton X-100 and stained with DAPI. Fluorescence images were acquired using a confocal laser scanning microscope (LSM 510; Zeiss, Oberkochen, Germany).

**Annexin V/PI staining for apoptosis**—Cellular apoptosis was measured with FITC Annexin V Apoptosis Detection Kit I (BD PharMingen, San Diego, CA, USA) as per as manufacturer’s protocol. In brief, HeyA8 and OVCAR5 cells were reverse transfected with siRNAs (siCont and siFXR1). After 48h, the cells were trypsinized, washed with PBS and resuspended in Annexin V binding buffer at a concentration of 10<sup>6</sup> cells/ml. Annexin V–FITC (5 µl) was added, vortex-mixed gently and incubated for 15 min at 4°C in the dark. Cells were stained with 5 µL of PI for another 5 min at 4°C in the dark. Stained cells were acquired on a FACS Calibur flow cytometer (Becton-Dickinson, Mansfield, MA) and data were analyzed with Flowjo software version 10.6.1 (TreeStar, Ashland, OR, USA).

**Caspase3/7 activity assay**—Following treatments with siFXR1s for 48h, cells were subjected to Caspase 3/7 activity measurement with Caspase-Glo assay kit (Promega, Madison USA). Briefly, the plates containing cells were removed from the incubator and allowed to equilibrate to room temperature for 30 minutes. 100 µL of Caspase-Glo reagent was added to each well, the content of well was gently mixed with a plate shaker at 300–500 rpm for 30 s. The plate was then incubated at room temperature for 2 hours. The luminescence of each sample was measured in SpectraMax i3x Multi-Mode Microplate Reader (Molecular Devices, Japan Co., Ltd., Tokyo, Japan).

**Human apoptosis protein array**—A human apoptosis array (Proteome Profiler Cat# ARY009; R&D Systems) was used to analyze apoptosis-related protein profiles according to manufacturer instructions. In brief, the total HeyA8 cell lysates after siFXR1-2 treatment (48h) were first incubated with the array membrane overnight at 4°C, followed by incubation with a biotinylated detection antibody cocktail at room temperature for 1 h. The membranes were then exposed and quantified by ImageJ software (National Institutes of Health, Bethesda, USA).

**Lentiviral FXR1 knockdown**—For viral creation, HEK293T cells were transfected with packaging vectors pLP1, pLP2 and VSVG plasmids including control empty vector pLKO.1 (Cat#SHC001V) and two different FXR1 targeting short hairpin RNA (shRNA) (TRC number 1: TRCN0000160812, Clone ID: NM\_005087.1-130s1c1; 2: TRCN0000160901, Clone ID: NM\_005087.1-579s1c1) purchased from Sigma-Aldrich (Saint Louis, MO). Competent lentiviruses were collected 48 h after transfection. HeyA8 cells were passaged to

40% confluence, the next day viral media were added to cells with 8 µg/ml of polybrene. Efficacy of individual FXR1 shRNA construct was checked by western blot analysis for FXR1 knockdown using FXR1 antibody (Cat#12295, Cell Signaling Technology). The most effective shRNA construct was used for generating FXR1 knockdown stable cell line by selection with puromycin (8 µg/ml; for 2 weeks). The clones were picked and subjected to expansion culture under further selection. Western blot analysis was performed to identify the stable clone with most efficiently downregulated FXR1 protein, which was used in further experiments.

**Transfections for forced and inducible FXR1 and cMYC overexpression**—To establish the stable overexpression of FXR1 in OVCAR3 cells, we transfected the cells with control vector or pReceiver-M39 vector expressing FXR1 (GeneCopoeia, Rockville, MD) using Lipofectamine 2000 (Invitrogen, Carlsbad, CA). Cells were selected 4h after transfection to ensure that the cells were stably incorporated with control sequences or FXR1 using puromycin (2.5 µg/ml) containing culture media for two weeks. Western blotting was performed to check the expression of FXR1 and other targets in stable cells followed by colony formation assay for 12 days.

To create the tetracycline inducible cell line, HeyA8 cells were plated in a 6-well dish and transfected with pTRE-Tight GFP FXR1-expressing plasmid constructed at Vector Core facility, Varsity Blood Research Institute using lentivirus method as mentioned above. GFP positive cells were selected by FACS sorting after tetracycline (Takara Bio Inc., San Francisco, CA, USA) treatment (1µg/ml). Transduced cells were expanded and used for further experiments.

**RPPA assay and data processing**—Reverse Phase Protein Array (RPPA) and data analysis was performed as previously described (Hennessy et al., 2010) and detailed at the MD Anderson Cancer Center RPPA core facility as below: <https://www.mdanderson.org/research/research-resources/core-facilities/functional-proteomics-rppa-core.html>

Briefly, cells were washed in ice-cold PBS, and lysed in 30 µL of RPPA lysis buffer [1% Triton X-100, 50 nmol/L HEPES (pH 7.4), 150 nmol/L NaCl, 1.5 nmol/L MgCl<sub>2</sub>, 1 mmol/L EGTA, 100 nmol/L NaF, 10 nmol/L NaPPi, 10% glycerol, 1 nmol/L PMSF, 1 nmol/L Na<sub>3</sub>VO<sub>4</sub>, and protease inhibitor cocktail] for 30 minutes with frequent vortexing on ice, followed by centrifuging for 15 min at 14,000 rpm, and the supernatant were collected. Protein concentration was determined by Pierce BCA Protein Assay kit (Thermo Fisher Scientific, Waltham, MA) with a BSA standard curve according to manufacturer's protocol. 30 µL lysates were transferred into a 96-well PCR plate. To each sample well, 10 µL of SDS/2-ME sample buffer (35% glycerol, 8% SDS, 0.25 mol/L Tris-HCl, pH 6.8; with 10% β-mercaptoethanol) was added and incubated for 5 minutes at 95°C and then centrifuged for 1 minute at 2,000 rpm.

Samples were diluted serially and transferred into 384-well plates and heated at 95°C for 10 min. Approximately, 1 nL of protein lysate was then printed onto nitrocellulose-coated glass slides (FAST Slides, Schleicher & Schuell BioScience, Inc., Keene, NH) with an automated robotic GeneTac arrayer (Genomic Solutions, Inc., Ann Arbor, MI) per array by

pin touch. Each spot on the array slide represents a certain dilution of the lysate of a sample. Following slide printing, the array slides were blocked for endogenous peroxidase prior to the addition of the primary antibody, then treated with biotinylated secondary antibody (anti-mouse or anti-rabbit) was used as a starting point for signal amplification. Tyramide-bound horseradish peroxidase cleaves 3,3'-diaminobenzidine tetrachloride, giving a stable brown precipitate with excellent signal-to-noise ratio. Signal intensity was captured by scanning the slides with ImageQuant (Molecular Dynamics, Sunnyvale, CA) and quantified using the MicroVigene automated RPPA module unit (VigeneTech, Inc., North Billerica, MA). The intensity of each spot was calculated, and an intensity concentration curve was calculated with a slope and intercept using MicroVigene software.

**Protein decay and mRNA half-life analysis**—For cMYC protein stability experiments, after treatment of HeyA8 and Kuramochi cells with siCont and siFXR1-2 for 48 h, 25 µg/ml of CHX was added to inhibit protein synthesis and samples were collected at every 20 minutes for 140 min. For the experiments with FXR1 overexpression, stable HeyA8 cells expressing Tet-FXR1 were treated with CHX and processed as previously described for western blotting and quantified by densitometry.

The level of cMYC transcript was measured by qRT-PCR in HeyA8 and Kuramochi cells treated or untreated with FXR1-siRNA for 48h, HeyA8 cells expressing Tet-FXR1, OVCAR3 cells with CRISPR/Cas9-mediated ARE knockout in cMYC 3'UTR followed by treatment with actinomycin D (5µg/ml) for various times, respectively. Normalized CTs values from each sample were used to calculate the remaining percentage of cMYC mRNA at each point. We fit these data into a first-phase decay model to derive mRNAs' half-life.

**RNA immunoprecipitation (RIP) assay**—RIP assay was performed using Magna RIP RNA-Binding Protein Immunoprecipitation Kit (Millipore Sigma, Burlington, MA) according to manufacturer's instructions. In brief, following whole cell protein extraction from OVCAR5, HeyA8 and Kuramochi cells lysates were incubated with respective antibodies coupled to Dynabeads Protein A/G for overnight at 4°C. Following extensive washes, the immobilized immunoprecipitated complexes were incubated with proteinase K at 55°C for 30 min to digest the protein. Co-precipitated RNA and the Input (crude lysate) were eluted and purified with Trizol Reagent and analyzed by qPCR. The primers used are listed in Table S1.

**In vitro translation assay**—*In vitro* translation assay for cMYC was performed by rabbit reticulocyte lysate system (Promega, USA) according to manufacturer's instructions. In brief, total RNA (1 µg/ml) from HeyA8 and Kuramochi cells was subjected to *in vitro* translation by addition to 35 µL of rabbit reticulocyte lysate, methionine-free amino acid mixture, 40U of RNasin, transcend tRNA, and 4 µg of purified human recombinant FXR1-GST protein (Novus Biologicals) for 1.5 h at 30°C. The reaction mixture was resolved by SDS-PAGE and cMYC translation was checked by western blot analysis using cMYC antibody (Cat# 5605S, Cell Signaling Technology).

**SUnSET assay**—HeyA8 cells were transfected with siFXR1-2 and after 48 hours incubated with 10mg/ml puromycin (Cat# A1113803, Thermo Fisher Scientific) in time

dependent manner. Likewise, OVCAR3 cells with FXR1 overexpression were seeded and incubated with puromycin (10µg/ml). Cells were washed with PBS to remove residual puromycin and collected by scraping. Cells were lysed using 1x RIPA buffer lysates and run on an SDS-PAGE gel, transferred to a nitrocellulose membrane for western blotting with anti-puromycin antibody (Millipore, Cat#MABE343). Puromycin staining in lanes was measured using chemiluminescence kit (Pierce, Rockford, IL).

For flow cytometry, HeyA8 cells were transfected with siCont or siFXR1-2 for 48h and treated with CHX (50µg/ml) for 1h followed by with incubation with 10µg/ml puromycin for 10min. Cells were washed with PBS to remove residual puromycin followed by staining of cells using Alexa fluor-488 anti-puromycin antibody (Millipore, Cat#MABE343-AF488).

**Co-immunoprecipitation**—For immunoprecipitation, Dynabeads® Co-immunoprecipitation Kit including Dynabeads® M-270 Epoxy beads were used (Thermo Fisher Scientific, MA, USA). 5mg of beads/IP were conjugated with respective antibodies (FXR1 Proteintech, Cat#13194-1-AP), eIF4A1 Sigma-Aldrich, Cat# SAB2700953, eIF4E, Sigma-Aldrich Cat# E5906, eIF4G, Santa Cruz Biotechnology Cat# 3344) overnight at 37°C with shaking. Antibody conjugated beads were added to cell lysates and allowed to incubate on a rotator for four hours at 4°C. Following incubation, beads were removed and washed with cold lysis buffer, boiled, and analyzed by western blot.

For RFP-trap pull-down assay, HeyA8 cells were transfected with RFP-tagged FXR1<sup>FL</sup>, and mutants (FXR1<sup>Tud1</sup>, FXR1<sup>Tud2</sup>, FXR1<sup>- RGG</sup> and FXR1<sup>C</sup>) plasmid constructed at Vector Core facility, Versity Blood Research Institute through viral transfection, collected 36h after transfection and washed with PBS prior to lysis. Cells were lysed for 15 min on ice in buffer (50 mM Tris-HCl pH 7.5 at 4°C, 100 mM NaCl, 0.1% NP-40, 1 mM DTT) supplemented with protease inhibitors (complete, EDTA-free Protease inhibitor cocktail, Roche). Cell lysates were cleared at 16,000 g for 15 min at 4°C and supernatants were supplemented with 5 µl/ml of RNase A/T1 (Thermo Fisher Scientific) for 30 min at 4°C. After clearing the lysate again at 16,000 g for 15 min, 12-20 µL of RFP-TRAP Dynabeads beads (Chromotek, NY, USA) were added to the supernatants and the mixtures were rotated for 1 hour at 4°C. Beads were washed with ice-cold RFP-trap dilution buffer. and proteins were eluted in sample buffer by boiling at 95°C for 10 min followed by western blotting.

**Immunostaining**—Immunostaining was performed as described previously (Chaluvally-Raghavan et al., 2014; Pradeep et al., 2014). Briefly, HeyA8 cells were grown on eight-well chamber slides (ibidi USA, Madison, WI, USA) then fixed with 4% paraformaldehyde and permeabilized with 0.1% Triton X-100 in blocking solution (0.5% BSA in PBS) followed by blocking for 1 h with 0.5% BSA in PBS, and then stained overnight at 4°C with the indicated primary antibodies. After washing with PBS, cells were incubated with secondary antibodies, Alexa Fluor goat anti-mouse 488 (Cat#38731, Life Technologies, Carlsbad, CA) and Alexa Fluor 568 goat anti-rabbit (Cat#35646, Life Technologies, Carlsbad, CA) for 1 hour at room temperature. Glass slides were mounted using ProLong Gold Antifade Reagent (Life Technologies, Carlsbad, CA) containing DAPI. Images were acquired with a 40X objective using a confocal laser scanning microscope (LSM 510; Zeiss, Oberkochen, Germany) and analyzed using the Aim 4.2 software LSM510.

**m<sup>7</sup>GTP pull-down assay**—For pull-down assay, 20  $\mu$ l m<sup>7</sup>GTP agarose beads were added to each tube and washed with IP buffer (Tris-HCl pH 7.5 50 mM, NaCl 150 mM, EDTA 1 mM, EGTA 1 mM, Triton X-100 1%, and NP-40 0.5%) three times. Quantified protein extracts prepared from whole cell lysates were then added on top of the m<sup>7</sup>GTP agarose beads at equal amounts in each tube and were incubated with beads on the rotator overnight at 4 °C. Western blotting was performed to determine the association of candidate proteins with m<sup>7</sup>G cap.

**Polysome fractionation by sucrose gradients**—Polysome fractionation was performed following a previously published protocol (Gandin et al., 2014). In brief, HeyA8 cells were transfected with siFXR1-2 for 48hrs and total lysate was prepared by scraping in hypotonic buffer (5 mM Tris-HCl, pH 7.5, 2.5 mM MgCl<sub>2</sub>, 1.5 mM KCl and 1x protease inhibitor cocktail) supplemented with 100  $\mu$ g/ml cycloheximide (CHX), 1 mM DTT, and 100 units of RNAase inhibitor. Triton X-100 and sodium deoxycholate were added to a final concentration of 0.5% each, and samples were vortexed for 5 s. Samples were centrifuged at 16,000 g for 7 min at 4°C. Supernatants (cytosolic cell extracts) were collected and absorbance at 254 nm was measured. Approximately 10-15 OD<sub>260</sub>s of lysate was layered over 5% – 50% cold sucrose gradients in buffer (200 mM HEPES (Ph 7.6), 50 mM MgCl<sub>2</sub>, 1 mM KCl, 100  $\mu$ g/mL CHX and 1x protease inhibitor, 100 units of RNAase inhibitor). Gradients were centrifuged at 39,000 rpm in a Beckman SW28 rotor for 2 h at 4°C. After centrifugation, 14 equal-sized fractions (0.75 mL/fraction) were collected and analyzed through UV detection. For western blotting, fractions were precipitated with 95% alcohol and mixed with SDS sample buffer. For qPCR, total RNA was isolated from the fractions by mixing with phenol:chloroform:isoamyl alcohol (Sigma-Aldrich) and then RNA was analyzed by qRT-PCR.

**Bioluminescence optical imaging**—The IVIS Lumina II Bioluminescence and Fluorescence Imaging System (Caliper Life Sciences) was used for *in vivo* bioluminescent imaging. Mice were injected (i.p.) with 150  $\mu$ g/kg body weight D-luciferin substrate (Gold Biotechnology, St. Louis, MO) and imaging was performed 10 min later (the peak time point). Images of the tumor were taken under the following settings: exposure time = 0.5 s, f/stop = 16, medium binning, field of view = 12.5  $\times$  12.5 cm<sup>2</sup>. Living Image software was used to quantify the bioluminescent signals, reported as units of tissue radiance (photons/s/cm<sup>2</sup>/sr).

To further obtain the whole body three-dimensional (3D) images of mice to monitor tumor growth and metastasis, fluorescence Positron Emission Tomography-computed tomography (PET-CT) imaging (Perkin Elmer, Shelton, CT) was performed, and images/videos were captured using Living Image software.

**RNA electrophoretic mobility shift assay (REMSA)**—Biotin labeled and unlabeled RNA oligonucleotides probes corresponding to the human cMYC ARE (1-6) and two random probes (R1, R2) were synthesized as indicated in Table S6 by Sigma-Aldrich. REMSA was performed with a LightShift chemiluminescent RNA EMSA Kit (Thermo Fisher Scientific) following the manufacturer's instruction. Briefly, purified human FXR1-GST protein (5 mg/ml) (Novus Biologicals, USA) and purified human GST protein

(5 mg/ml) (Sigma-Aldrich) were incubated for 30min with biotinylated probes (100 pM) in REMSA binding buffer and glycerol. In competition binding assays, unlabeled RNA oligonucleotides (Sigma-Aldrich) were added in increasing amounts (200-fold) and incubated for another 10 min at room temperature. RNA/protein complexes were then subjected to electrophoresis by 6% native polyacrylamide gel and transferred to nylon membrane (Thermo Fisher Scientific). RNA was cross-linked with a UV lamp at a distance of 0.5 cm from the membrane for 2 min. The membrane was blocked in blocking buffer for 15 min and replaced the blocking buffer with conjugate/blocking buffer. After washed with 1 × wash buffer for 3 times, membrane was incubated in substrate equilibration buffer for 5 min. Then, the membrane was incubated in working solution and exposed.

**Proximity ligation assay**—The DuoLink® *In Situ* Red Starter Kit Mouse/Rabbit (Sigma-Aldrich) was used to detect proximity between FXR1 protein and *cMYC* mRNA according to manufacturer protocol. Briefly, HeyA8 and Kuramochi cells were transiently transfected with 5' FAM-labeled oligonucleotides (n = 6, Table S7) synthesized by GenScript (Piscataway, NJ, USA) and after 24h of transfection, reseeded in eight-well chamber slides (ibidi USA, Madison, WI, USA) and cultured overnight. Slides were washed with cold 1 × PBS and fixed in 4% paraformaldehyde for 30 min. Then slides were blocked with Duolink Blocking Solution in a pre-heated humidified chamber for 1hr at 4°C and followed by hybridizations with probes targeting *cMYC* RNAs (Table S8), respectively at 37°C. The primary antibodies to detect FXR1 (Proteintech, Cat#13194-1-AP) and biotin (Cat# 07-599, Rockland) was added to the slides and incubated overnight at 4°C. Then slides were washed with 1 × Wash Buffer A and subsequently incubated with the PLA probes (1:5 diluted in antibody diluents) for 1h, then the Ligation-Ligase solution for 30 min, and the Amplification-Polymerase solution for 100 min in a pre-heated humidified chamber at 37°C. Before imaging, slides were washed with 1 × Wash Buffer B and mounted with a coverslip using Duolink *In Situ* Mounting Medium with DAPI. Fluorescence images were acquired using a confocal laser scanning microscope (LSM 510; Zeiss, Oberkochen, Germany).

**Dual-luciferase reporter assay**—The full-length (FL) *cMYC* 3' UTR (NCBI Reference Sequence: NM\_001354870.1; 3' UTR region: 2523-4515) and four mutants (M1-M4) with base substitution in certain AREs cloned into a pEZX-MT06 dual-luciferase Target Expression Vector were provided by GeneCopoeia (GeneCopoeia, Rockville, MD, USA). A vector without *cMYC* 3' UTR (GeneCopoeia) was used as experimental control. To mutate the ARE regions in the *cMYC* 3' UTR, the sequence ARE regions was replaced as indicated (Figure 6; Table S9). OVCAR3 cells with stable FXR1 overexpression were transiently transfected with luciferase vectors (a luciferase vector containing the full-length (FL) *cMYC* 3' UTR and luciferase vectors containing the mutants (M1-M4)) with Lipofectamine 2000 Reagent (Thermo Fisher Scientific). After 48h, the luciferase activity was measured by using the Dual-Luciferase Reporter Assay System (GeneCopoeia, USA). Data were presented as the ratios between the Firefly and Renilla luminescence activities.

**CRISPR/Cas9-mediated ARE deletion in *cMYC* 3' UTR of ovarian cancer cells**—CRISPR/Cas9-mediated ARE knockout in *cMYC* 3' UTR of OVCAR3 cells was created at Synthego Inc (Menlo Park, CA, USA). The sgRNA sequences were used

as follows: TCAGTCTCAAGACTCAGCCA/TATAAGCCTCTGAAAACCTA. Deletion of ARE in cMYC 3'UTR cells was validated by sequencing of the PCR amplified edited fragment using the primers and gel electrophoresis after extracting the genomic DNA. Sequencing primers were used as follows: F: CCAAGCAGAGGAGCAAAAGC R: ACAGGGAGCTGAAG ACCTACT. Wild-type (WT) and ARE knockout OVCAR3 cells were transiently transfected first with pReceiver-M39 vector expressing FXR1 (GeneCopoeia, Rockville, MD) and pEZX-MT06 vector expressing cMYC 3'UTR (GeneCopoeia) for 48h using Lipofectamine 2000 (Invitrogen, Carlsbad, CA) followed by colony formation and western blot analysis using the indicated antibodies.

**Copy number variation analysis**—Genome-wide copy number variation data of ovarian cancer and breast cancer were downloaded from Broad GDAC Firehose (<https://gdac.broadinstitute.org/>). GISTIC2 was used to identify genomic regions that are significantly gained or lost across a set of tumors. A '+2/-2' indicates that the sample had high-level copy number amplification or deletion. We defined the copy number amplification/deletion frequency as the number of patients with copy number amplification/deletion divided the total number of patients sequenced. The copy number of all patients across 3q26.33 was plotted as heatmap using the R package heatmap (<https://cran.r-project.org/web/packages/heatmap/index.html>)

**Gene set enrichment analysis (GSEA)**—Gene expression data of ovarian cancer, breast cancer, LUAD and LUSC were obtained from TCGA project. The expressions of protein coding genes were measured by fragments per kilobase of exon model per million reads mapped (FPKM). The expression of each gene was log<sub>2</sub> transformed and then we calculated the Pearson Correlation Coefficient (PCC) between the expression of all other genes and FXR1. All genes were ranked based on PCC and then subjected to GSEA analysis (Subramanian et al., 2005). The enrichment score (ES) was calculated for each functional set, which reflects the degree to which a gene set is overrepresented at the top or bottom of the ranked list of genes. Moreover, the normalized enrichment score (NES) was calculated based on 1000 permutations. Here, the cancer hallmark gene sets from MSigDB were considered for the names and the gene sets with false discovery rate < 0.001 were considered as a selection criteria (Liberzon et al., 2015).

**Clinical data analysis using cBioPortal**—TCGA data datasets were first analyzed using cBioPortal (<http://www.cbioportal.org/>). The segmented data for all the samples were downloaded from the TCGA Firehose (<http://firebrowse.org>, version: 20160128), followed by standard GISTIC2 (Genomic Identification of Significant Targets in Cancer, version 2) analysis using Firehose-suggested parameters. We evaluated the protein expression of FXR1 in multiple cancers by Clinical Proteomic Tumor Analysis Consortium (CPTAC) analysis using UALCAN data portal (<http://ualcan.path.uab.edu/>).

**Survival Analysis**—Tothill ovarian cancer dataset (Tothill et al., 2008) was downloaded from GEO database (<https://www.ncbi.nlm.nih.gov/gds>) for survival analysis. Cox proportional hazard regression model was used for univariate survival analysis. Overall survival or Recurrence free Survival (RFS) was used as endpoint. The cut-offs of the

high-expression and low-expression groups were optimized to achieve the lowest p value. Student's t test was used to compare the gene expressions between different gene mutation types. All statistical analysis was performed using R Software (<http://www.r-project.org/>). Progression-free survival (PFS) was defined as the time interval between the date of diagnosis and the first confirmed sign of disease recurrence based on Gynecologic Cancer Intergroup (GCIg) criteria (Vergote et al., 2000). Overall survival (OS) was defined as the time interval between the date of histological diagnosis and the date of death from any cause. Patients who died from causes deemed unrelated to their malignancy were censored for survival analysis.

**Functional enrichment analysis**—Differentially expressed genes were analyzed in the context of biological functions, pathways, and diseases using the Ingenuity Pathway Analysis software (IPA; Ingenuity Systems Inc). The p value was calculated using Fisher's exact test to determine a potential significant association between differentially expressed proteins and specific functional categories. A p value < 0.05 was considered to be statistically significant. Subsequently, sets of differentially expressed proteins from RPPA were applied to STRING software (Search Tool for the Retrieval of Interacting Genes/Proteins; STRING Consortium) for interaction predictions.

## QUANTIFICATION AND STATISTICAL ANALYSIS

In most cases, data obtained from three or four biological replicates were analyzed, unless indicated otherwise in the Figure legends. Statistical significance defined as a P value < 0.05 or < 0.01 was determined by unpaired Student's t test. Comparisons in multiple groups were analyzed with one-way or two-way analysis of variance (ANOVA), which is mentioned in the respective Figure legends. Data are presented as the mean  $\pm$  standard error (SEM) as indicated in the Figure legends. For the analysis of correlation co-efficient, Pearson's correlation coefficients (r) were calculated. Heatmaps were prepared with heatmapper software <http://www.heatmapper.ca/>. GraphPad Prism 7 (GraphPad, San Diego, CA) was used to perform statistical analysis and p value determinations.

**Additional resources**—There are no additional resources associated with this study.

## Supplementary Material

Refer to Web version on PubMed Central for supplementary material.

## ACKNOWLEDGMENT

Authors acknowledge Dr. Dinah Singer, Center for Cancer Research, National Cancer Institute for her guidance and feedback on translational assays. This work was supported in part by funding from the Ovarian Cancer Research Fund Alliance (OCRFA) (to P.C.-R. and S.P.), the Women's Health Research Program (WHRP) at MCW (to P.C.-R. and S.P.), MCW Cancer Center institutional research grants from the American Cancer Society (16-183-31 to P.C.-R. and 14-247-29 to Y.S.), and research funds from MCW Cancer Center. Critical support was also received from the NCI R01CA229907 and DoD W81XWH-21-1-0365 to P.C.-R., R01CA188575 to H.R., NIGMS 1R01GM124183 to M.D., the National Natural Science Foundation of China 31970646 to Y. L., and P50CA217685, P50 CA098258, the American Cancer Society Research Professor Award, and the Frank McGraw Memorial Chair in Cancer Research to A.K.S.

## REFERENCES

- Baker VV, Borst MP, Dixon D, Hatch KD, Shingleton HM, and Miller D (1990). c-myc amplification in ovarian cancer. *Gynecol. Oncol* 38,340–342. [PubMed: 2227545]
- Borman AM, Michel YM, Malnou CE, and Kean KM (2002). Free poly(A) stimulates capped mRNA translation in vitro through the eIF4G-poly(A)-binding protein interaction. *J. Biol. Chem* 277, 36818–36824. [PubMed: 12138105]
- Cancer Genome Atlas Research Network (2011). Integrated genomic analyses of ovarian carcinoma. *Nature* 474, 609–615. [PubMed: 21720365]
- Cao H, Gao R, Yu C, Chen L, and Feng Y (2019). The RNA-binding protein FXR1 modulates prostate cancer progression by regulating FBXO4. *Funct. Integr. Genomics* 19, 487–496. [PubMed: 30746571]
- Chaluvally-Raghavan P, Zhang F, Pradeep S, Hamilton MP, Zhao X, Rupaimoole R, Moss T, Lu Y, Yu S, Pecot CV, et al. (2014). Copy number gain of hsa-miR-569 at 3q26.2 leads to loss of TP53INP1 and aggressiveness of epithelial cancers. *Cancer Cell* 26, 863–879. [PubMed: 25490449]
- Chaluvally-Raghavan P, Jeong KJ, Pradeep S, Silva AM, Yu S, Liu W, Moss T, Rodriguez-Aguayo C, Zhang D, Ram P, et al. (2016). Direct Up-regulation of STAT3 by MicroRNA-551b-3p Deregulates Growth and Metastasis of Ovarian Cancer. *Cell Rep.* 15, 1493–1504. [PubMed: 27160903]
- de la Parra C, Ernlund A, Alard A, Ruggles K, Ueberheide B, and Schneider RJ (2018). A widespread alternate form of cap-dependent mRNA translation initiation. *Nat. Commun* 9, 3068. [PubMed: 30076308]
- Fatscher T, Boehm V, Weiche B, and Gehring NH (2014). The interaction of cytoplasmic poly(A)-binding protein with eukaryotic initiation factor 4G suppresses nonsense-mediated mRNA decay. *RNA* 20, 1579–1592. [PubMed: 25147240]
- Gabay M, Li Y, and Felsher DW (2014). MYC activation is a hallmark of cancer initiation and maintenance. *Cold Spring Harb. Perspect. Med* 4, a014241. [PubMed: 24890832]
- Gandin V, Sikström K, Alain T, Morita M, McLaughlan S, Larsson O, and Topisirovic I (2014). Polysome fractionation and analysis of mammalian translatoemes on a genome-wide scale. *J. Vis. Exp* (87)
- Glisovic T, Bachorik JL, Yong J, and Dreyfuss G (2008). RNA-binding proteins and post-transcriptional gene regulation. *FEBS Lett.* 582, 1977–1986. [PubMed: 18342629]
- Harvey R, Dezi V, Pizzinga M, and Willis AE (2017). Post-transcriptional control of gene expression following stress: the role of RNA-binding proteins. *Biochem. Soc. Trans* 45, 1007–1014. [PubMed: 28710288]
- Hennessy BT, Lu Y, Gonzalez-Angulo AM, Carey MS, Myhre S, Ju Z, Davies MA, Liu W, Coombes K, Meric-Bernstam F, et al. (2010). A Technical Assessment of the Utility of Reverse Phase Protein Arrays for the Study of the Functional Proteome in Non-microdissected Human Breast Cancers. *Clin. Proteomics* 6, 129–151. [PubMed: 21691416]
- Jung M, Russell AJ, Kennedy C, Gifford AJ, Mallitt KA, Sivarajasingam S, Bowtell DD, DeFazio A, Haber M, Norris MD, et al. ; Australian Ovarian Cancer Study Group (2018). Clinical Importance of Myc Family Oncogene Aberrations in Epithelial Ovarian Cancer. *J. Natl. Cancer Inst. Cancer Spectr* 2, pky047.
- Kirkpatrick LL, McIlwain KA, and Nelson DL (1999). Alternative splicing in the murine and human FXR1 genes. *Genomics* 59, 193–202. [PubMed: 10409431]
- Landen CN Jr., Chavez-Reyes A, Bucana C, Schmandt R, Deavers MT, Lopez-Berestein G, and Sood AK (2005). Therapeutic EphA2 gene targeting in vivo using neutral liposomal small interfering RNA delivery. *Cancer Res.* 65, 6910–6918. [PubMed: 16061675]
- Li Y, Casey SC, and Felsher DW (2014). Inactivation of MYC reverses tumorigenesis. *J. Intern. Med* 276, 52–60. [PubMed: 24645771]
- Li XC, Song MF, Sun F, Tian FJ, Wang YM, Wang BY, and Chen JH (2018). Fragile X-related protein 1 (FXR1) regulates cyclooxygenase-2 (COX-2) expression at the maternal-fetal interface. *Reprod. Fertil. Dev* 30, 1566–1574. [PubMed: 29852926]

- Liberzon A, Birger C, Thorvaldsdóttir H, Ghandi M, Mesirov JP, and Tamayo P (2015). The Molecular Signatures Database (MSigDB) hallmark gene set collection. *Cell Syst.* 1, 417–425. [PubMed: 26771021]
- Majumder M, House R, Palanisamy N, Qie S, Day TA, Neskey D, Diehl JA, and Palanisamy V (2016). RNA-Binding Protein FXR1 Regulates p21 and TERC RNA to Bypass p53-Mediated Cellular Senescence in OSCC. *PLoS Genet.* 12, e1006306. [PubMed: 27606879]
- Parashar D, Geethadevi A, Aure MR, Mishra J, George J, Chen C, Mishra MK, Tahiri A, Zhao W, Nair B, et al. (2019). miRNA551b-3p Activates an Oncostatin Signaling Module for the Progression of Triple-Negative Breast Cancer. *Cell Rep.* 29, 4389–4406.e10. [PubMed: 31875548]
- Pradeep S, Kim SW, Wu SY, Nishimura M, Chaluvally-Raghavan P, Miyake T, Pecot CV, Kim SJ, Choi HJ, Bischoff FZ, et al. (2014). Hematogenous metastasis of ovarian cancer: rethinking mode of spread. *Cancer Cell* 26, 77–91. [PubMed: 25026212]
- Qian J, Hassanein M, Hoeksema MD, Harris BK, Zou Y, Chen H, Lu P, Eisenberg R, Wang J, Espinosa A, et al. (2015). The RNA binding protein FXR1 is a new driver in the 3q26–29 amplicon and predicts poor prognosis in human cancers. *Proc. Natl. Acad. Sci. USA* 112, 3469–3474. [PubMed: 25733852]
- Ruggero D (2013). Translational control in cancer etiology. *Cold Spring Harb. Perspect. Biol* 5, a012336. [PubMed: 22767671]
- Schmidt EK, Clavarino G, Ceppi M, and Pierre P (2009). SUnSET, a nonradioactive method to monitor protein synthesis. *Nat. Methods* 6, 275–277. [PubMed: 19305406]
- Sekulovski N, MacLean JA, Bheemireddy SR, Yu Z, Okuda H, Pru C, Plunkett KN, Matzuk M, and Hayashi K (2021). Niclosamide's potential direct targets in ovarian cancer. *Biol. Reprod* 105, 403–412. [PubMed: 33855343]
- Shayesteh L, Lu Y, Kuo WL, Baldocchi R, Godfrey T, Collins C, Pinkel D, Powell B, Mills GB, and Gray JW (1999). PIK3CA is implicated as an oncogene in ovarian cancer. *Nat. Genet* 21, 99–102. [PubMed: 9916799]
- Subramanian A, Tamayo P, Mootha VK, Mukherjee S, Ebert BL, Gillette MA, Paulovich A, Pomeroy SL, Golub TR, Lander ES, and Mesirov JP (2005). Gene set enrichment analysis: a knowledge-based approach for interpreting genome-wide expression profiles. *Proc. Natl. Acad. Sci. USA* 102, 15545–15550. [PubMed: 16199517]
- Tohill RW, Tinker AV, George J, Brown R, Fox SB, Lade S, Johnson DS, Trivett MK, Etemadmoghadam D, Locandro B, et al. ; Australian Ovarian Cancer Study Group (2008). Novel molecular subtypes of serous and endometrioid ovarian cancer linked to clinical outcome. *Clin. Cancer Res* 14, 5198–5208. [PubMed: 18698038]
- Truitt ML, and Ruggero D (2016). New frontiers in translational control of the cancer genome. *Nat. Rev. Cancer* 16, 288–304. [PubMed: 27112207]
- Vasudevan S, and Steitz JA (2007). AU-rich-element-mediated upregulation of translation by FXR1 and Argonaute 2. *Cell* 128, 1105–1118. [PubMed: 17382880]
- Vergote I, Rustin GJ, Eisenhauer EA, Kristensen GB, Pujade-Lauraine E, Parmar MK, Friedlander M, Jakobsen A, and Vermorken JB (2000). Re: new guidelines to evaluate the response to treatment in solid tumors [ovarian cancer]. *Gynecologic Cancer Intergroup. J. Natl. Cancer Inst* 92, 1534–1535. [PubMed: 10995813]
- Wang W, Cortes JE, Lin P, Beaty MW, Ai D, Amin HM, McDonnell TJ, Ok CY, Kantarjian HM, Medeiros LJ, and Hu S (2015). Clinical and prognostic significance of 3q26.2 and other chromosome 3 abnormalities in CML in the era of tyrosine kinase inhibitors. *Blood* 126, 1699–1706. [PubMed: 26243778]

### Highlights

- CNVs of FXR1 associate with its expression in ovarian cancer
- FXR1 promotes the survival and proliferation of ovarian cancer cells
- FXR1 binds to AU-rich elements (ARE) within 3'UTR of cMYC
- FXR1 promotes the recruitment of eIF4F complex to translation initiation site

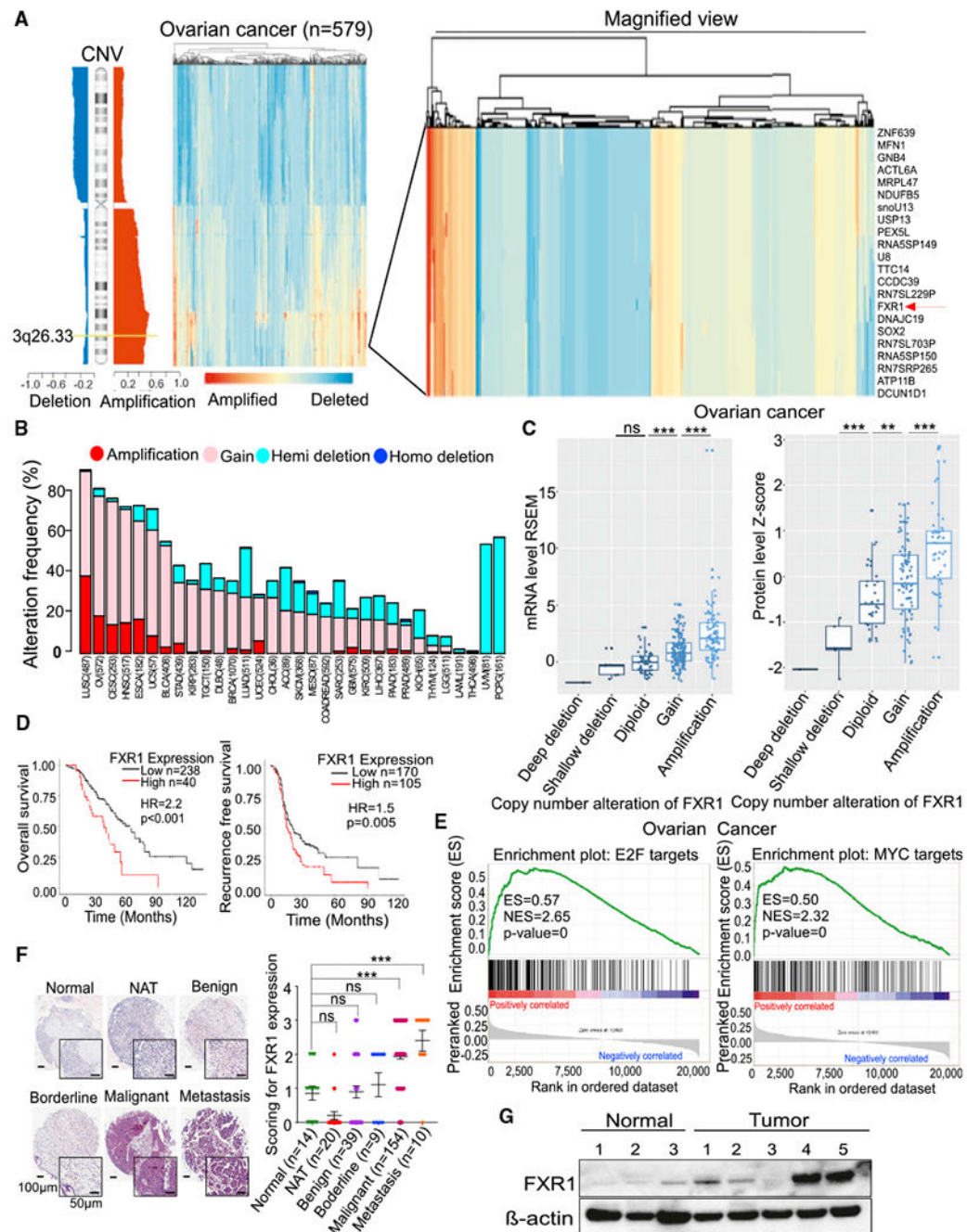


**Figure 1. *FXR1* mRNA and protein associated with the progression of ovarian cancer**  
 (A) Heatmap of chromosome 3q26.3 locus amplification in TCGA ovarian cancer patient's dataset (n = 579). Representative genes in this amplicon are magnified; red arrow indicates position of *FXR1*.  
 (B) Frequency of *FXR1* alterations across human cancers in TCGA database.  
 (C) Boxplots show the association of copy number alterations of *FXR1* with *FXR1* mRNA (left panel) and *FXR1* protein (right panel). These considered with respect to the median expression of all data in the TCGA ovarian cancer data. Error bars indicate median  $\pm$  SD.

p value was determined by two-sided Wilcoxon rank-sum test. Number of samples (n) for deep deletion is 1, shallow deletion is 7, diploid is 49, gain is 157, and amplification is 86 for mRNA analysis. n for deep deletion is 1, shallow deletion is 5, diploid is 33, gain is 82, and amplification is 47 for protein analysis.

(D) Kaplan-Meier plot shows FXR1 expression-based outcome of overall survival and recurrence-free survival in 278 patients with ovarian cancer in the Tothill et al. (2008) (Bowtell) dataset. Patients were stratified according to the median expression of FXR1. p value was determined by log-rank test.

(E) GSEA analysis demonstrates the ES of indicated functional annotation marks based on the correlation between expression of all genes and FXR1 expression in the TCGA ovarian cancer samples. ns, non-significant; ES, enrichment score; NES, normalized enrichment score.

(F) IHC analysis of ovarian cancer tissue microarray (TMA) was performed for FXR1. Vector Red chromogen staining was performed and IHC scoring was performed based on the positive staining of FXR1 (red color). Tissue cores were blindly scored for FXR1 staining intensity as negative (0), trace, weak (1+), moderate (2+), or strong (3+) in 50% of the cells examined. Scale bars, 100 and 50  $\mu\text{m}$ , respectively. Black squares indicate enlarged images. Error bars indicate SEM. \* $p < 0.05$ , \*\*\*\* $p < 0.0001$  compared to normal tissues by unpaired Student's t test. ns, non-significant. See also Figure S1E and Tables S1, S2, and S3.

(G) Western blot analysis of FXR1 levels in normal patients and patients with ovarian cancer tissue.  $\beta$ -actin, loading control.

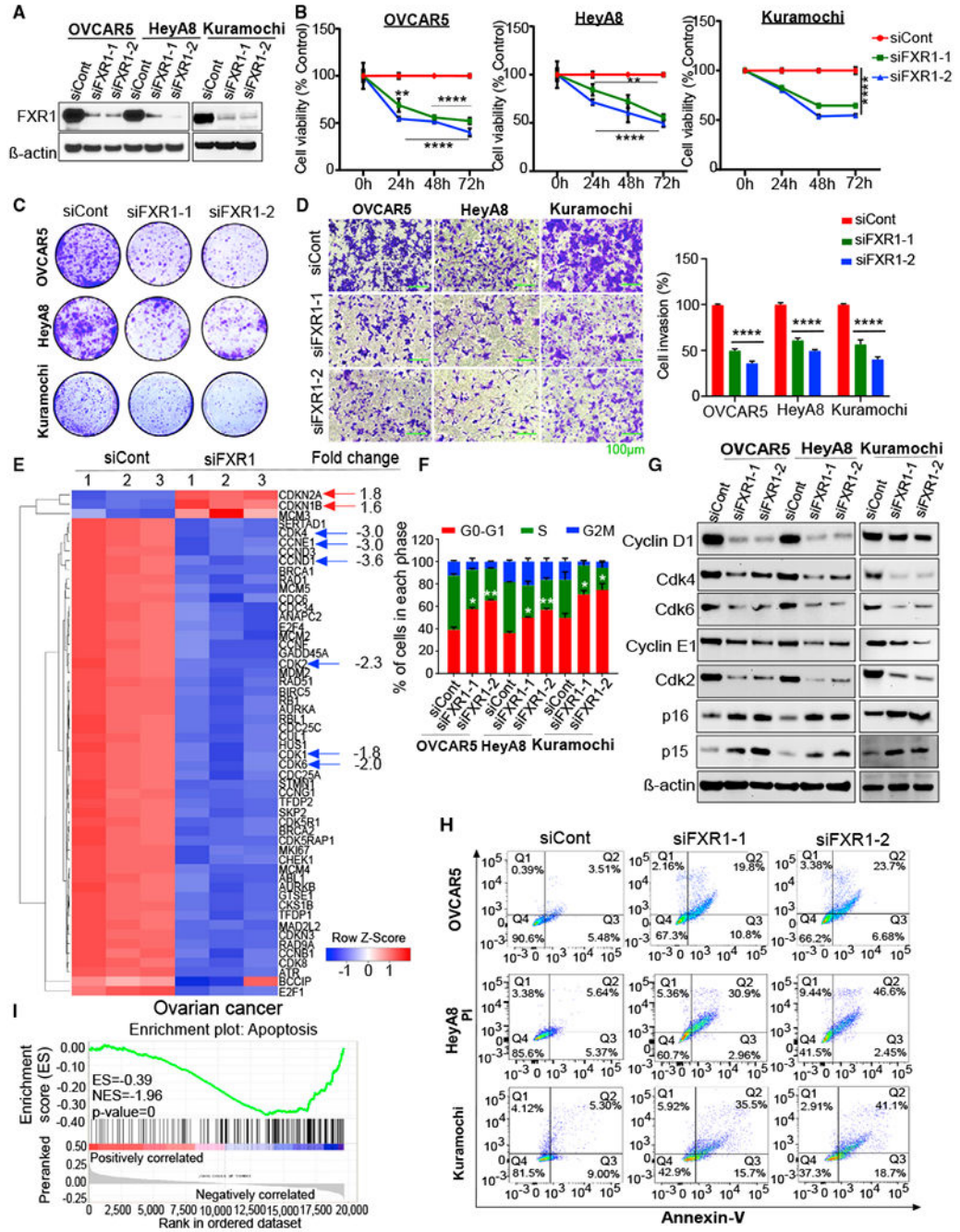


**Figure 2. FXR1 knockdown inhibited the growth of ovarian cancer cells by promoting the apoptosis.**

(A) Ovarian cancer cells were transfected with two different siRNAs targets FXR1 (siFXR1-1 and siFXR1-2) or control siRNAs (siCont), and western blot was performed 48 h after transfection using antibodies indicated.  $\beta$ -actin, loading control.

(B) Ovarian cancer cells were transfected using the siRNAs and cell viability was determined using the CCK-8 assay at indicated time points.

(C and D) Ovarian cancer cells were transfected using the siRNAs as in (A) and subjected to (C) colony formation assay and (D) invasion assay. Scale bar, 100  $\mu$ m.

(E) qPCR array was performed using the cDNA prepared from the HeyA8 cells that were transfected with siCont or siFXR1. Gene expression is represented as Log<sub>2</sub> of Ct values and with  $p > 0.05$  compared to siCont. Genes ( $n = 54$ ) that were 1.5-fold downregulated (blue color) or upregulated (red color) were included in the heatmap.

(F) Flow cytometry analysis of the cell cycle of ovarian cancer cells transfected with siRNAs.

(G) Western blots of the lysates of cells from (F) were performed using the antibodies indicated.  $\beta$ -actin, loading control.

(H) Cells transfected with siCont or FXR1 siRNAs were double-stained with annexin V-FITC and PI and then subjected to flow cytometric analysis after 48 h of transfection.

(I) GSEA analysis demonstrates the ES of indicated functional annotation marks based on FXR1 expression in the TCGA ovarian cancer samples.

Error bars indicate mean  $\pm$  SEM. Significance was determined by Student's t test, where \* $p < 0.05$ , \*\* $p < 0.01$ , \*\*\*\* $p < 0.0001$ ,  $n = 5$  (B), and  $n = 3$  (D and F). ES, enrichment score; NES, normalized enrichment score.

See also Figure S2 and Table S4.

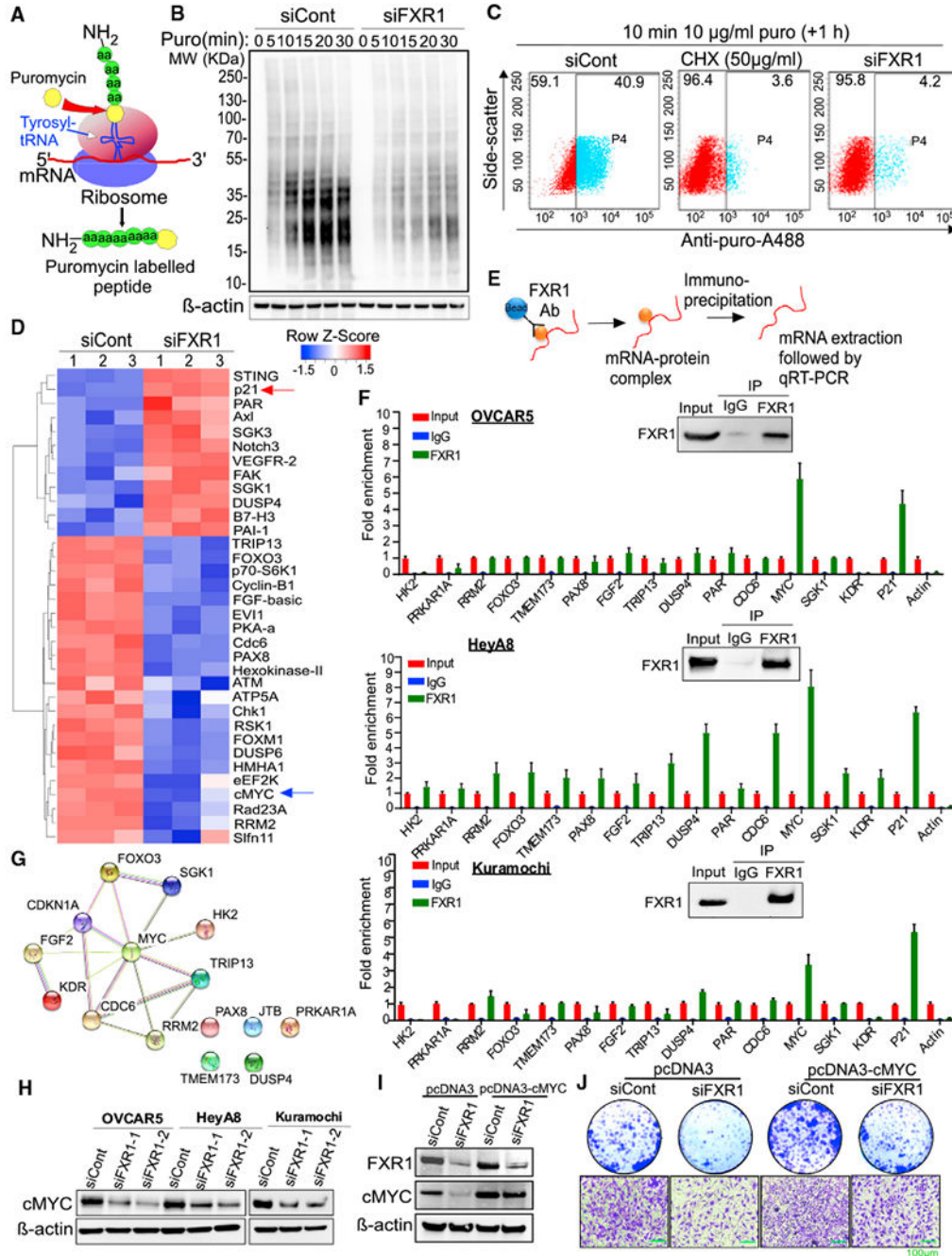


**Figure 3. FXR1 alters the overall protein translation and promotes the levels of cMYC protein** (A) Schema illustrates the principle of surface sensing of translation (SUNSET) assay on how puromycin acts as a structural analog of tyrosyl-tRNA incorporated in a growing peptide chain. (B) Western blot analysis of proteins labeled with puromycin (puro) using anti-puromycin antibody in time-dependent manner in HeyA8 cells were transfected with either siCont or siFXR1.  $\beta$ -actin, loading control.

(C) FACS of the puromycin-labeled cells using the anti-puromycin antibody tagged with Alexa Fluor 647 in the HeyA8 cells were transfected with either siCont or siFXR1 or treated with cycloheximide (CHX).

(D) Heatmap of the differentially expressed proteins based on Log<sub>2</sub> fold change (n = 34) identified by reverse phase protein array (RPPA) analysis with a p value of <0.05 compared to siCont. Normalized Log<sub>2</sub> values of RPPA signal were used in this analysis. Blue and red values represent down- and upregulated proteins, respectively.

(E) A schema presents how the RNA immunoprecipitation (RNA-IP) assay was performed to verify the direct interaction between selected mRNAs and FXR1 by using monoclonal antibody specific to FXR1.

(F) Total RNA was eluted from the RNA-IP, and qPCR was performed for the enrichment of *cMYC* mRNA in ovarian cancer cells. Bottom: analysis was done by quantitating *cMYC* mRNA in the complex immunoprecipitated compared to control IgG. Top: representative western blot of FXR1 in the corresponding samples. Error bars indicate mean ± SEM, n = 3.

(G) Protein-protein interaction enrichment network generated in STRING using the 15 significantly altered proteins from RPPA. The edges represent protein-protein association. Blue and pink edges are known interactions (from curated databases and experimentally determined, respectively). Light green and black edges are interactions derived from text mining and co-expression, respectively. The red and green edge is a predicted interaction as gene neighborhood.

(H) Ovarian cancer cells were transfected with indicated siRNAs and immunoblot analysis was performed using the lysates prepared after 48 h of transfection using indicated antibodies. β-actin, loading control.

(I) HeyA8 cells were transfected with *cMYC* CDS without its 3'UTR cloned in pCDNA3 or its vector control 24 h after the transfection of either control or FXR1 siRNA. Cells were then lysed 48 h after the *cMYC* CDS transfection, and immunoblot was performed. β-actin, loading control.

(J) Cells from (I) were subjected to colony formation and invasion assay. Scale bar, 100 μm See also Figure S3.

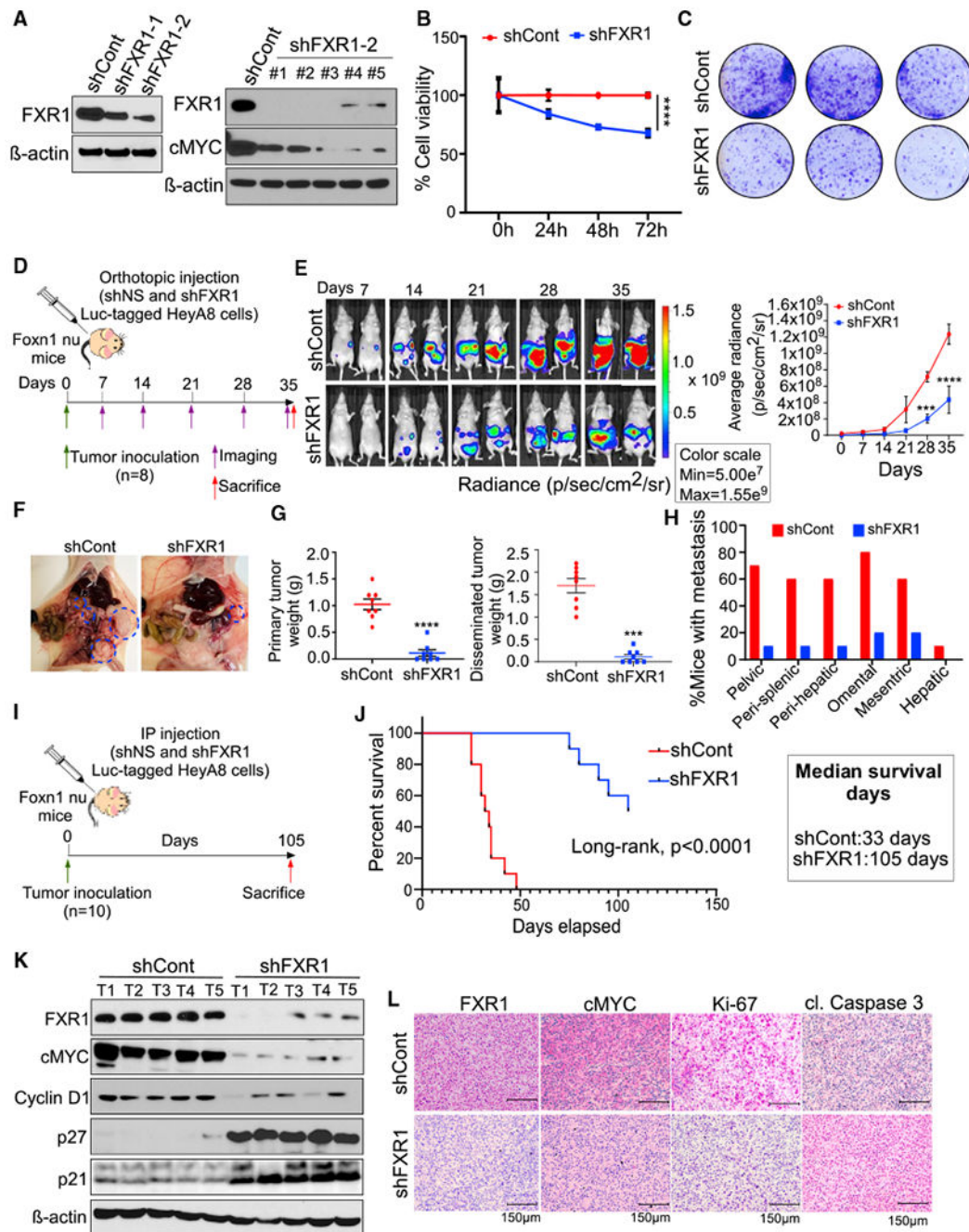


**Figure 4. Stable knockdown of FXR1 reduced the overall tumor growth, metastasis, and prolonged survival of ovarian xenograft mouse model**

(A) Western blot analysis for confirming the knockdown of FXR1 in HeyA8 cells prepared using pLKO.1 vector express two independent shRNA constructs of FXR1 (1: TRCN0000160812 and 2: TRCN0000160901) or empty control pLKO.1 vector (shCont) (left). Lysates were prepared from the colonies (shFXR1 1–5) and immunoblotted using the antibodies indicated (right). β-actin, loading control.

(B) Cell survival rate of shCont and shFXR1 HeyA8 cells were determined using the CCK-8 assay at the indicated time point.

(C) Stable cells from (A) were plated and the colonies formed were photographed on day 10.

(D) Timeline of establishment of ovarian cancer xenograft mouse models using  $25 \times 10^3$  luciferase tagged HeyA8 cells (shCont and shFXR1) were orthotopically inoculated into the left ovary bursa of female athymic nude mice ( $n = 8/\text{group}$ , green arrow).

(E) Mice from both groups were imaged using biophotonic IVIS at the indicated time points and representative photographs were presented (left). Line graph indicates the average radiance of signaling intensity (right).

(F) Representative image of a mouse from shCont and shFXR1 groups were surgically opened and photographed. Areas circled in blue indicate tumor growth and metastatic locations.

(G) Primary and disseminated tumors were collected from (E) and total tumor weight was recorded.

(H) Bar graph shows the percentage of mice with metastasis in the indicated organs in both shCont and shFXR1 groups.

(I) Schema shows the plan and timeline we used for survival analysis.  $25 \times 10^3$  luciferase-tagged HeyA8 cells (shCont or shFXR1) were intraperitoneally (i.p.) inoculated into female athymic nude mice ( $n = 10/\text{group}$ , green arrow).

(J) Kaplan-Meier analysis was performed using the death record of mice from each group in (I).

(K) Western blot analysis of lysates was collected from tumor tissues selected from each group ( $n = 5$ ) using indicated antibodies.  $\beta$ -actin, loading control.

(L) Representative images (20 $\times$  magnification) of indicated antibodies prepared using the ovarian tumor tissues collected from shCont and shFXR1 mice from (I). Scale bar, 150  $\mu\text{m}$  Error bars indicate mean  $\pm$  SEM. Significance was determined by Student's t test, two-way ANOVA test, and log-rank test, where \*\*\* $p < 0.001$  and \*\*\*\* $p < 0.0001$ .  $n = 3$  (B),  $n = 8$  (D–H), and  $n = 10$  (I and J).

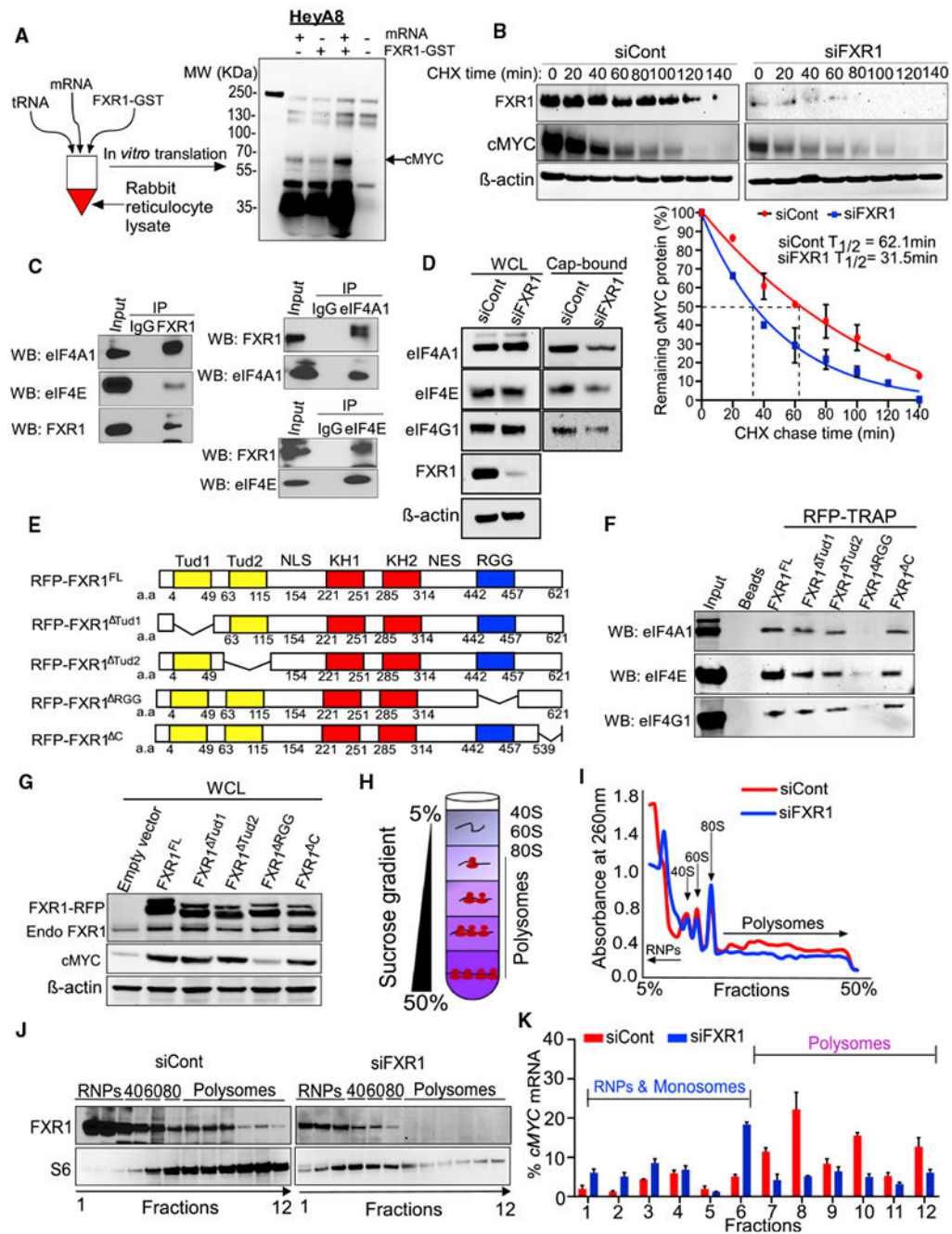


**Figure 5. FXR1 stabilizes cMYC post-transcriptionally and interacts with eukaryotic initiation factors (eIFs) for translation**

(A) *In vitro* translation assay was performed using the total RNA isolated from HeyA8 and Kuramochi cells, which were then incubated with FXR1-GST human recombinant protein for 1.5 h then immunoblotted using cMYC antibody.

(B) Immunoblot was performed using the lysates prepared from the HeyA8 cells that were transfected with siCont or siFXR1 for 48 h, followed by the treatment with CHX (25 μg/mL) for indicated time points (left). β-actin, loading control. Densitometric quantification

measurements of cMYC protein bands from the blots were quantitated using Image-J and analyzed for phase decay quantification (right).

(C) HeyA8 cell lysates were immunoprecipitated using indicated antibodies. The immunocomplexes were then eluted and immunoblotted for indicated proteins. Normal immunoglobulin G (IgG) was used as the negative control and 5% whole lysates (Input) was used as the positive control.

(D) HeyA8 cells were transfected with control siRNA or FXR1 siRNAs for 48 h, and lysates were incubated with m<sup>7</sup>GTP (5' mRNA cap analog). Cap-associated proteins were then eluted and immunoblotted using the antibodies indicated.

(E) A schematic representation of full-length (FXR1<sup>FL</sup>) and various mutants of FXR1 protein.

(F) HeyA8 cells were transfected with RFP-tagged FXR1<sup>FL</sup> and mutants. After 48 h, cells were harvested and lysed, and protein complexes were isolated on RFP-Trap Dynabeads. The immunocomplexes were then eluted and immunoblotted using indicated antibodies. Empty beads were used as the negative control, and 5% whole lysates (Input) were used as the positive control.

(G) The presence of FXR1 and cMYC in whole cell lysates (WCL) of empty control vector, FXR1<sup>FL</sup>, and mutants was analyzed by western blotting.  $\beta$ -actin, loading control.

(H) Schema represents how we performed the polysome profiling using sucrose gradient (5%–50%) columns to collect fractions of RNAs bound to the ribosome units as indicated.

(I) Plot of the absorbance profile of fractions obtained through sucrose gradients to isolate polysomes from HeyA8 cells transfected with control siRNAs or siFXR1 for 48 h. Peaks and curves indicate the binding of RNA to the marked units of ribosome or polysome.

(J) Western blot analysis of the protein fractions isolated from (I) was performed using the antibodies indicated.

(K) qPCR shows the enrichment of *cMYC* mRNA in the isolated fractions bound with free RNPs, monosomes, and polysomes. Data were normalized with the control group.

Error bars indicate mean  $\pm$  SEM. Domain abbreviations: Tud, Tudor; NLS, nuclear localization sequence; NES, nuclear export sequence; KH, K homology; RGG, arginine-glycine-glycine repeat. n = 3 (B, lower panel, and K)

See also Figure S5.

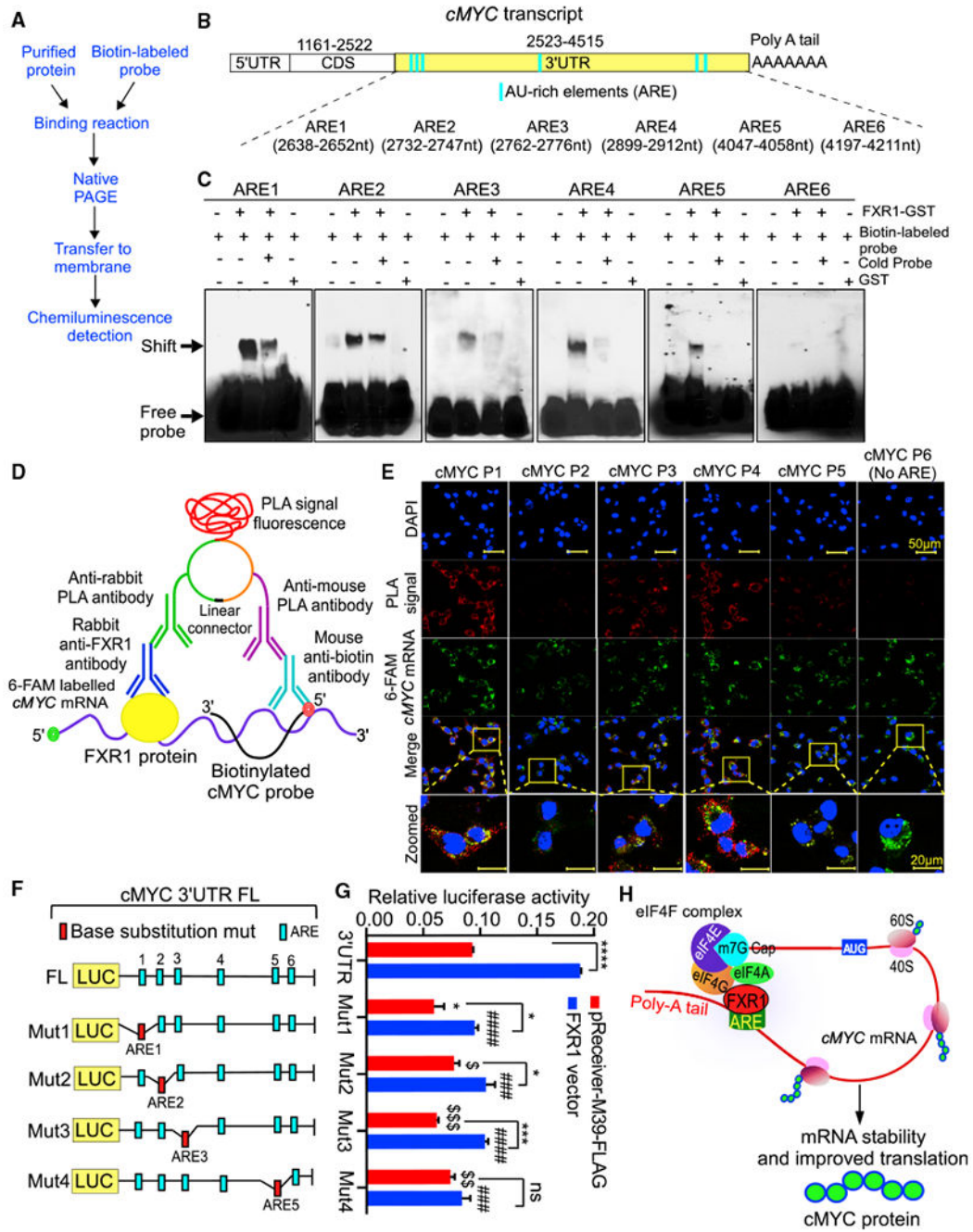


**Figure 6. FXR1 binds to the AU-rich elements (ARE) in *cMYC* 3'UTR for translation**

(A) Work flow for RNA electromobility shift assay (REMSA).

(B) Schema shows the number (ARE1 to ARE6) and position of ARE in the whole 3'UTR of *cMYC* transcript.

(C) Biotinylated RNA probes containing 15-mer of human *cMYC* AREs were incubated with GST or FXR1-GST human recombinant protein for 30 min. For competition assay, biotinylated RNA probes were mixed along with or without 200-fold of unlabeled *cMYC* probes. Reaction mixtures were then resolved on 6% gel and blotted to nylon membrane and

developed by chemiluminescence assay. Arrow marks indicate the position of free probe and shift in the mobility due to FXR1 binding.

(D) Schema of RNA-proximity ligation assay (PLA) demonstrate the proximal localization of FXR1 protein with *cMYC* mRNA.

(E) Representative fluorescence images ( $\times 40$  magnification) of HeyA8 cells, previously transfected with 5'FAM-labeled *cMYC* mRNA oligonucleotides ( $n = 6$ ) and then reseeded, fixed, permeabilized, and incubated with anti-FXR1 antibody and oligonucleotide probes anti-sense to 3'UTR of *cMYC* ( $n = 6$ ). PLA was performed to detect the interaction of FXR1 protein and the *cMYC* mRNA (yellow merge color); nuclei were stained with DAPI (blue). Scale bar, 20  $\mu\text{m}$

(F) Map of full-length or mutated *cMYC* 3'UTR was prepared and cloned in the downstream of luciferase reporter in pEZX-MT06 vector. Red marks indicate base substitution mutations in the ARE sequence.

(G) Each of the *cMYC* 3'UTR constructs in (F) were transfected in the OVCAR3 cells, which stably express FXR1 or control vector, then the luciferase reporter activity was measured 24 h after transfection in the cell lysates using a plate reader.

(H) Proposed model demonstrates that how FXR1 binding on 3'UTR of *cMYC* facilitate the translation by recruiting the eIF4F factors to translation initiation site. Error bars indicate mean  $\pm$  SEM. Significance was determined by Student's t test, where \* $p < 0.05$ , \*\*\* $p < 0.001$ , and \*\*\*\* $p < 0.0001$  compared with empty control vector; ### $p < 0.001$  and #### $p < 0.0001$  compared to *cMYC* FL 3'UTR FXR1 vector; and \$ $p < 0.05$ , \$\$ $p < 0.01$ , and \$\$\$ $p < 0.001$  compared to empty control vector.  $n = 3$  (G). ns, non-significant.

See also Figures S6 and S7.

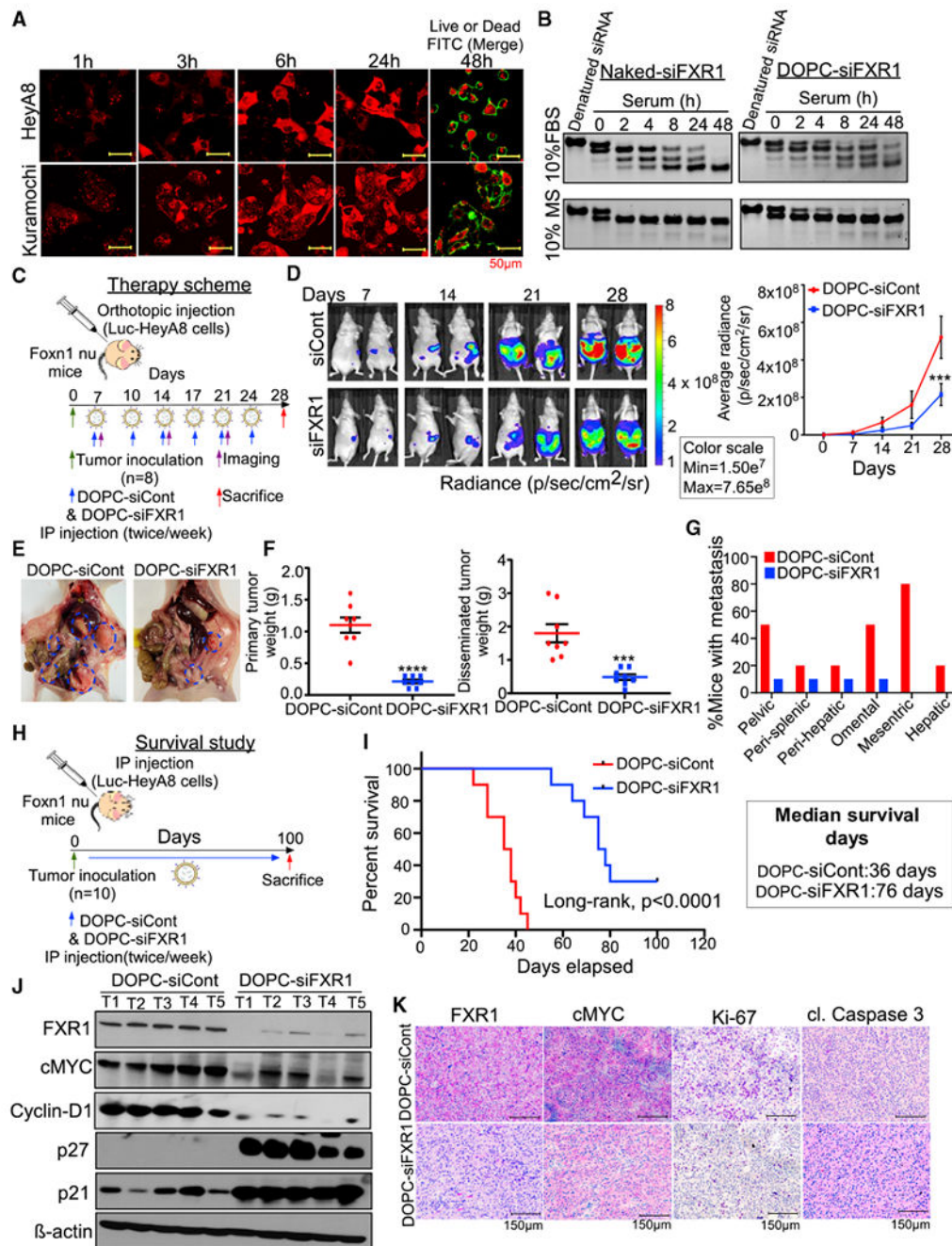


**Figure 7. Systemic administration of siFXR1 encapsulated nanoliposome inhibited tumor growth and metastasis of ovarian cancer in ovarian xenograft mouse models**

(A) HeyA8 ovarian cancer cells were transfected with FXR1 siRNA labeled with Texas red, and its cellular uptake was determined by confocal microscopy. siFXR1 transfected cells were treated with Live-or-Dye 488/515 (FITC) to quantitate cell death (green fluorescence). Scale bar, 50  $\mu$ m

(B) The different siRNAs were incubated in 10% FBS or 10% mouse serum at 37°C, and aliquots were taken at the time points indicated. siRNAs were then separated by PAGE and visualized with ethidium bromide.

(C) Timeline of establishment of ovarian cancer xenograft mouse models using HeyA8 cells-tagged with luciferase reporter ( $25 \times 10^3$ ) inoculated into the left ovary bursa of female athymic nude mice orthotopically ( $n = 8/\text{group}$ , green arrow) with a treatment schedule of 1,2-dioleoyl-sn-phosphatidylcholine (DOPC)-control siRNA or DOPC-siFXR1 treatment at a concentration of  $150 \mu\text{g}/\text{kg}$  body weight (blue arrow; twice a week for 4 weeks). Purple arrow indicates days of imaging.

(D) Mice ( $n = 8$ ) were imaged using an IVIS imager, and representative images of two mice per group were presented at the indicated time point (left). Bioluminescent signals were quantitated at the indicated time points and presented (right).

(E) Representative image of the anatomy of peritoneal cavity of mice were treated with DOPC-siCont or DOPC-siFXR1 as shown in (C). Areas circled in blue indicate tumor nodule formed in each peritoneal organ.

(F) Primary and disseminated tumors were collected from (E), and total tumor weight was recorded.

(G) Bar graph shows the percentage of mice with metastasis in the indicated organs in both DOPC-siCont- or DOPC-siFXR1-treated groups.

(H) Schema shows the plan and timeline we used for survival study. HeyA8 cells-tagged with luciferase reporter ( $25 \times 10^3$ ) were intraperitoneally (i.p.) inoculated into female athymic nude mice ( $n = 10/\text{group}$ , green arrow), and DOPC-siCont or DOPC-siFXR1 was given twice a week for 5 weeks.

(I) Kaplan-Meier analysis was performed using the death record of mice from each group in (G).

(J) Western blot analysis of lysates was collected from representative tumor tissues collected from each group ( $n = 5$ ) from (C).  $\beta$ -actin, loading control.

(K) Representative images of immunohistochemistry of ovarian tumor tissues collected from DOPC-siCont-and DOPC-siFXR1-treated group from (C). Scale bar,  $150 \mu\text{m}$ .

Error bars indicate mean  $\pm$  SEM. Significance was determined by Student's t test, two-way ANOVA test, and log-rank test where \*\*\* $p < 0.001$  and \*\*\*\* $p < 0.0001$ .  $n = 8-10$  (C-I).

## KEY RESOURCES TABLE

REAGENT or RESOURCE	SOURCE	IDENTIFIER
Antibodies		
Alexa Fluor 568 goat anti-rabbit	Life Technologies	Cat# F2765, RRID: AB_10562896
Alexa Fluor goat anti-mouse 488	Life Technologies	Cat# F2761, RRID: AB_1500661
anti-Biotin	Rockland	Cat# 200-301-098, RRID: AB_2611059
anti-puromycin	Millipore	Cat# MABE343, RRID: AB_2566826
Anti-Puromycin	Sigma Aldrich	Cat# MABE343; RRID: AB_2566826
Anti-Puromycin, clone 12D10, Alexa Fluor® 488 Conjugate	Millipore	Cat# MABE343-AF488; RRID: AB_2736875
Anti-rabbit IgG, HRP-linked	Cell Signaling Technology	Cat# 7074P2, RRID: AB_2099233
Bax	Cell Signaling Technology	Cat# 2772, RRID: AB_10695870
Bcl2	Santa Cruz Biotechnology	Cat# sc-7382, RRID: AB_626736
Cdk2	Cell Signaling Technology	Cat# 2546, RRID: AB_2276129
Cdk4	Cell Signaling Technology	Cat# 12790, RRID: AB_2631166
Cdk6	Cell Signaling Technology	Cat# 13331, RRID: AB_2721897
Cleaved caspase3	Cell Signaling Technology	Cat# 9669, RRID: AB_2069869
cMYC	Cell Signaling Technology	Cat# 5605S; RRID: AB_1903938
cMYC	Santa Cruz Biotechnology	Cat# sc-47694; RRID: AB_627266
Cyclin D1	Cell Signaling Technology	Cat# 12205, RRID: AB_2797845
Cyclin E1	Cell Signaling Technology	Cat# 20808, RRID: AB_2783554
DYKDDDDK Tag (D6W5B) Rabbit mAb	Cell Signaling Technology	Cat# 14793S; RRID: AB_2572291
eIF4A1	Sigma-Aldrich	Cat# SAB1300839, RRID: AB_10606599
eIF4E	Sigma-Aldrich	Cat# E5906, RRID: AB_796203
eIF4G1	Proteintech	Cat# 15704-1-AP, RRID: AB_2261979
FXR1	Cell Signaling Technology	Cat# 12295S; RRID: AB_2797875
FXR1	Proteintech	Cat# 13194-1-AP; RRID: AB_2110702
FXR1	Santa Cruz Biotechnology	Cat# sc-374148; RRID: AB_10918113
Ki-67	Cell Signaling Technology	Cat# 9027, RRID: AB_2636984
p21 Waf1/Cip1	Cell Signaling Technology	Cat# 2947, RRID: AB_823586
p27 Kip1	Cell Signaling Technology	Cat# 3686, RRID: AB_2077850
Rabbit (DA1E) mAb IgG XP® Isotype Control	Cell Signaling Technology	Cat# 8726S; RRID: AB_10828938
S6 Ribosomal Protein	Cell Signaling Technology	Cat# #2217, RRID: AB_331355
β-actin	Cell Signaling Technology	Cat# 4970, RRID: AB_2223172
RFP	Invitrogen	Cat# MA5-15257, RRID: AB_10999796
Biological samples		
Human ovarian cancer tissues	Medical College of Wisconsin	Protocol Number: PRO00033433
Normal ovarian and fallopian tube tissues	Medical College of Wisconsin	Protocol Number: PRO00033433
Chemicals, peptides, and recombinant proteins		
10% Formalin fixative	VWR	Cat# 16004-121

REAGENT or RESOURCE	SOURCE	IDENTIFIER
Acetic acid	Sigma Aldrich	Cat# A6283
Ampicillin	Sigma Aldrich	Cat# A5354
Anhydrotetracycline	Takara Bio USA	Cat# 631310
Antibiotic (Penicillin/Streptomycin)	Thermo Fisher Scientific	Cat# 15140122
Crystal Violet	Sigma Aldrich	Cat# C6158
Cycloheximide	Sigma Aldrich	Cat# 239765
DMEM	Thermo Fisher Scientific	Cat# 10569010
DMSO	Sigma Aldrich	Cat# D8418
Doxycycline	Sigma Aldrich	Cat# D9891
DPX mountant	Sigma Aldrich	Cat# 06522
Dynabeads Protein A	Invitrogen	Cat# 10001D
EDTA	Invitrogen	Cat# AM9260G
EGF	Invitrogen	Cat# PHG0314
Ethyl Alcohol	Sigma Aldrich	Cat# E7023
FBS	Atlanta Biologicals	Cat# H17112
Recombinant Human FXR1 Protein	Novus Biologicals	Cat# H00008087-Q01
GST Protein	Sigma Aldrich	Cat# SRP5348
Glutaraldehyde	Sigma Aldrich	Cat# G7651
Glycerol	Sigma Aldrich	Cat# G5516
Glycine	Sigma Aldrich	Cat# G8898
Hematoxylin Solution, Harris Modified	Sigma Aldrich	Cat# HHS32-1L
HEPES	Thermo Fisher Scientific	Cat# 15630080
Hydrogen Peroxide	Sigma Aldrich	Cat# 88597
IHC Antigen Retrieval solution	IHC World	Cat# IW-1100
KCl	Sigma Aldrich	Cat# P9333
LB Agar	Sigma Aldrich	Cat# L2897
LB Broth (Lennox)	Sigma Aldrich	Cat# L3022
Lipofectamine 2000	Thermo Fisher Scientific	Cat# 11668027
Matrigel	Corning	Cat# 354230
MCDB105	Invitrogen	Cat# M6395
Medium 199	Invitrogen	Cat#12340-030
Methanol	Sigma Aldrich	Cat# 34860
MgCl <sub>2</sub>	Sigma Aldrich	Cat# M8266
Mitomycin C	Sigma Aldrich	Cat# M4287
NP40	Thermo Fisher Scientific	Cat# 85124
Paraformaldehyde	Sigma Aldrich	Cat# 158127
PBS	Sigma Aldrich	Cat# P3813
Phenol:chloroform:isoamyl alcohol	Sigma Aldrich	Cat# 77619
Polybrene Transfection Reagent	Millipore	Cat# TR-1003

REAGENT or RESOURCE	SOURCE	IDENTIFIER
ProLong Gold Antifade Mountant with DAPI	Invitrogen	Cat# P36931
Protease inhibitor cocktail	Sigma Aldrich	Cat# P8340
Puromycin	Thermo Fisher Scientific	Cat# A1113803
RIPA buffer	Thermo Fisher Scientific	Cat# 89900
RNAiMax Transfection Reagent	Thermo Fisher Scientific	Cat# 13778030
RNase A	Invitrogen	Cat# AM2271
SDS	Sigma Aldrich	Cat # L4509
Sodium deoxycholate	Sigma Aldrich	Cat# D6750
Sucrose	Sigma Aldrich	Cat# S7903
Transcend (TM) tRNA	Promega	Cat# L5061
Triton X-100	Sigma Aldrich	Cat# T8787
Trypsin	Thermo Fisher Scientific	Cat# 15400054
Tween 20	Sigma Aldrich	Cat# P1379
Critical commercial assays		
Cell Counting Kit-8 (CCK-8) Assay	Dojindo Molecular Technologies	Cat# CK04-01
Pierce BCA Protein Assay kit	Thermo Fisher Scientific	Cat# 23227
RNeasy kit	QIAGEN	Cat# 74104
iScript cDNA synthesis kit	Bio-Rad	Cat# 1708891
iTaq Universal SYBR Green PCR Kit	Bio-Rad	Cat# 1725121
Luc-Pair Duo-Luciferase HS Assay Kit	GeneCopoeia	Cat# LF004
Caspase-Glo assay kit	Promega	Cat# G8090
Magna RIP™ RNA-Binding Protein Immunoprecipitation Kit	Millipore Sigma	Cat# 17-700
ABC-AP Kit	Vector Labs	Cat# AK-5000
Live-or-Dye 488/515 Fixable Staining Kit	Biotium	Cat# 32004-T
Vector Red Alkaline Phosphatase Substrate Kit I	Vector Labs	Cat# SK-5100
REMSA Kit	Thermo Fisher Scientific	Cat# 20158
PLA Kit ant-rabbit	Sigma Aldrich	Cat# DUO92002
PLA Kit anti-mouse	Sigma Aldrich	Cat# DUO92004
PLA Kit <i>in situ</i> detection reagent	Sigma Aldrich	Cat# DUO92008
Miniprep Kit	QIAGEN	Cat# 27104
Dynabeads® Co-immunoprecipitation Kit	Thermo Fisher Scientific	Cat# 14321D
Rabbit Reticulocyte Lysate System	Promega Corporation	Cat# L4960
M <sup>7</sup> GTP agarose beads	Creative Biomart	Cat# M <sup>7</sup> GTP-001A
RT <sup>2</sup> Profiler Human Cell Cycle PCR Array	QIAGEN	Cat# PAHS-020ZA
RT <sup>2</sup> Profiler Human Oncogenes and Tumor Suppressor PCR Array	QIAGEN	Cat# PAHS-502Z
Proteome Profiler Human Apoptosis Array Kit	R&D Systems	Cat# ARY009
RFP-TRAP Dynabeads beads	Chromotek	Cat# RTD010
Ovarian cancer tissue microarray	US Biomax	Cat# OV1005b

REAGENT or RESOURCE	SOURCE	IDENTIFIER
Ovarian cancer tissue microarray	US Biomax	Cat# OVC961
Ovarian cancer tissue microarray	US Biomax	Cat# OV1004
Deposited data		
Western blot RAW figures	Mendeley Data	<a href="https://data.mendeley.com/datasets/mgb7tv29jn/1">https://data.mendeley.com/datasets/mgb7tv29jn/1</a>
RPPA Dataset	Mendeley Data	<a href="https://doi.org/10.17632/jn296wnwff.1">https://doi.org/10.17632/jn296wnwff.1</a>
TCGA Ovarian Cancer Dataset	TCGA consortium portal	<a href="http://tcga-data.nci.nih.gov/tcga/findArchives.htm">http://tcga-data.nci.nih.gov/tcga/findArchives.htm</a>
TCGA Breast Cancer Dataset	TCGA consortium portal	<a href="http://tcga-data.nci.nih.gov/tcga/findArchives.htm">http://tcga-data.nci.nih.gov/tcga/findArchives.htm</a>
TCGA LUAD Cancer Dataset	TCGA consortium portal	<a href="http://tcga-data.nci.nih.gov/tcga/findArchives.htm">http://tcga-data.nci.nih.gov/tcga/findArchives.htm</a>
TCGA LUSC Cancer Dataset	TCGA consortium portal	<a href="http://tcga-data.nci.nih.gov/tcga/findArchives.htm">http://tcga-data.nci.nih.gov/tcga/findArchives.htm</a>
Tothill et al. (2008), Ovarian cancer dataset	Tothill et al., 2008	GSE9899
Experimental models: cell lines		
FTE188	MD Anderson Cancer Center	N/A
HEK293T	Thermo Scientific	N/A
HeyA8	MD Anderson Cancer Center	N/A
MCAS	MD Anderson Cancer Center	N/A
OVCAR3	NCI	Cat# OVCAR-3, RRID: CVCL_0465
OVCAR4	NCI	Cat# OVCAR-4, RRID: CVCL_1627
OVCAR5	NCI	Cat# OVCAR-5, RRID: CVCL_1628
OVCAR8	NCI	Cat# OVCAR-8, RRID: CVCL_1629
PEO1	Northwestern University	N/A
SKOV3	NCI	Cat# SK-OV-3, RRID: CVCL_0532
Kuramochi	Beth Israel Deaconess Medical Center	N/A
Experimental models: organisms/strains		
Athymic nude mice: CrTac: NCr-Foxn1 <sup>tm</sup>	Taconic	Cat# NCRNU-F; sp/sp
Oligonucleotides		
3' UTR target expression clone for Human MYC (see Table S9)	GeneCopia	Cat# HmiT102685-MT06
Biotinylated cMYC-REMSA probes (see Table S6)	Sigma Aldrich	N/A
FAM labeled oligonucleotides (see Table S7)	Genscript	N/A
Biotin labeled oligonucleotides (see Table S8)	Sigma Aldrich	N/A
FXR1 siRNA	Thermo Fisher Scientific	Cat# AM16708
siRNA Uni Negative Control	Sigma Aldrich	Cat# SIC001
mRNA Target clone control vector for pEZx-MT06	GeneCopia	Cat# CmiT000001-MT06
Mutant 1 mRNA 3' UTR target expression clone for Human MYC (see Table S9)	GeneCopia	Cat# CS-HmiT102685-MT06-01
Mutant 2 mRNA 3' UTR target expression clone for Human MYC (see Table S9)	GeneCopia	Cat# CS-HmiT102685-MT06-02

REAGENT or RESOURCE	SOURCE	IDENTIFIER
Mutant 3 mRNA 3'UTR target expression clone for Human MYC (see Table S9)	GeneCopia	Cat# CS-HmiT102685-MT06-03
Mutant 4 mRNA 3'UTR target expression clone for Human MYC (see Table S9)	GeneCopia	Cat# CS-HmiT102685-MT06-04
pReceiver-M39 control vector	GeneCopia	Cat# EX-EGFP-M39
pReceiver-M39 FXR1 vector	GeneCopia	Cat# EX-I1409-M39-GS
Primers for qPCR (see Table S1)	IDT	N/A
Software and algorithms		
CaseViewer Software	Thermo Fisher Scientific	<a href="https://www.3dhistech.com/">https://www.3dhistech.com/</a>
cBioPortal	cBioPortal	<a href="http://www.cbioportal.org/">http://www.cbioportal.org/</a>
FlowJo Software	Tree Star	<a href="https://www.flowjo.com/">https://www.flowjo.com/</a>
Gene Set Enrichment Analysis Software	Broad Institute	<a href="https://www.broadinstitute.org/gsea/index.jsp">https://www.broadinstitute.org/gsea/index.jsp</a>
GraphPad Prism 7	GraphPad Software	<a href="https://www.graphpad.com/scientific-software/prism/">https://www.graphpad.com/scientific-software/prism/</a>
ImageJ: J Coloc 2 image analysis plug-in	National Institutes of Health	<a href="https://imagej.net/plugins/coloc-2">https://imagej.net/plugins/coloc-2</a>
Ingenuity Pathway Analysis Software	QIAGEN	<a href="https://analysis.ingenuity.com">https://analysis.ingenuity.com</a>
Modfit LT 5.0 Software	Verity Software	<a href="http://www.vsh.com/products/mflt/index.asp">http://www.vsh.com/products/mflt/index.asp</a>
qPCR software	BioRad CFX Maestro	#12004110
UALCAN	UALCAN	<a href="http://ualcan.path.uab.edu/">http://ualcan.path.uab.edu/</a>